Contents lists available at ScienceDirect

Remote Sensing of Environment

journal homepage: www.elsevier.com/locate/rse

Simulation of SMAP and AMSR2 observations and estimation of multi-frequency vegetation optical depth using a discrete scattering model in the Tibetan grassland

Xiaojing Bai [a,b], Donghai Zheng [c,*], Xin Li [c], Jean-Pierre Wigneron [d], Rogier van der Velde [e], Pei Zhang [c,e], Zhongbo Su [e]

[a] School of Hydrology and Water Resources, Nanjing University of Information Science and Technology, Nanjing 210044, China
[b] Key Laboratory of Hydrometeorological Disaster Mechanism and Warning of Ministry of Water Resources, Nanjing University of Information Science and Technology, Nanjing 210044, China
[c] National Tibetan Plateau Data Center, State Key Laboratory of Tibetan Plateau Earth System, Resource and Environment, Institute of Tibetan Plateau Research, Chinese Academy of Sciences, Beijing 100101, China
[d] INRAE, UMR1391, ISPA, Université, de Bordeaux, F-33140 Villenave d'Ornon, France
[e] Faculty of Geo-Information Science and Earth Observation, University of Twente, Enschede, 7514AE, the Netherlands

ARTICLE INFO

ABSTRACT

Passive microwave observation at multiple frequencies has received increasing research interests due to its capability to provide comprehensive information of land surface properties. This paper contributes to the simulation of land surface emission and estimation of vegetation optical depth (VOD) at multiple frequencies using a discrete scattering model with a single set of model parameter values. Validity of the Tor Vergata (TVG) discrete scattering model in simultaneously reproducing the Soil Moisture Active Passive (SMAP) L-band (1.4 GHz) and Advanced Microwave Scanning Radiometer 2 (AMSR2) C- (6.925 GHz) and X-band (10.7 GHz) observations over the Tibetan grassland ecosystem is evaluated. Frequency-specific and multi-frequency calibration strategies are implemented to find the suitable set of model parameter values and to isolate the impact of frequency on parameter values. On this basis, the calibrated TVG model is further used to estimate the VOD, and to investigate the impact of microwave frequency and observation angle on the emission simulations and VOD parameterization.

The results show that both frequency-specific and multi-frequency calibration strategies achieve comparable and reasonable simulations of SMAP and AMSR2 observations, confirming the feasibility of using an identical physically-based model (i.e. the calibrated TVG model) to simulate multi-frequency land emission driven by a single set of model parameter values. As such, the dependence of emission components and VOD on frequency can be elaborated after isolating the impact of frequency on parameter values. The VOD values derived from the TVG simulations generally increase with increasing frequency and can be linearly correlated to the LAI variations, while current satellite-based retrievals have almost the same magnitude at the L-, C-, and X-band. The explanation for this can be that the retrieved VOD is different from the theoretical definition. Sensitivity test performed using the calibrated TVG model further shows that polarization-dependence of VOD becomes more apparent with the increasing observation angle and frequency. New parameterization has thus been developed to characterize the dependence of VOD on the frequency, observation angle, and polarization for grassland based on the results of sensitivity test. This study may provide new insights in improving model of land emission and retrievals of SM and VOD with physical interpretability based on multi-frequency satellite observations.

1. Introduction

Passive microwave remote sensing has been widely used for worldwide monitoring of land surface properties, such as surface soil moisture (SM) (Mecklenburg et al., 2016; Wigneron et al., 2017), vegetation optical depth (VOD) (Vittucci et al., 2016; Fernandez-Moran

---

et al., 2017; Li et al., 2020), vegetation scattering albedo (Konings et al., 2016, 2017), surface roughness (Karthikeyan et al., 2019), snow (Lemmetyinen et al., 2016), and irrigation (Zhang et al., 2022). Operational satellite missions/sensors using this technology include Soil Moisture Active Passive (SMAP) (Entekhabi et al., 2010) of National Aeronautic and Space Administration (NASA) launched in January 2015, Advanced Microwave Scanning Radiometer 2 (AMSR2) instrument (Imaoka et al., 2010) onboard the Japanese Aerospace Exploration Agency (JAXA) Global Climate Observing Mission-Water satellite (GCOM-W1) launched in May 2012, and Soil Moisture and Ocean Salinity (SMOS) (Kerr et al., 2001) of European Space Agency (ESA) launched in November 2009. Collectively, they observe the Earth microwave emission over a range of frequency bands centered at 1.4 GHz up to 89.0 GHz. By assuming negligible multiple scattering in vegetation canopy (Kurum et al., 2011), the observed total land surface emission comes from the direct upwelling vegetation emission, the upwelling soil emission attenuated by the canopy, and the downwelling vegetation emission reflected by the soil and attenuated by the canopy layer (Mo et al., 1982; Ferrazzoli and Guerriero, 1996; Wigneron et al., 2017). The relative contribution of each component largely depends on the wavelength of microwave signal and the optical density of vegetation canopy (Baur et al., 2019). At lower frequencies, the microwave radiations are better able to travel through vegetation (Fernandez-Moran et al., 2017) to provide a strong soil signal. On the contrary, microwave radiations at higher frequencies have less penetration into the vegetation, and their information comes mainly from the upper part of vegetation canopy. Therefore, satellite observations at multiple frequencies, as implemented by the planned European Copernicus Imaging Microwave Radiometer (CIMR) mission (Donlon, 2018), can provide complementary soil and vegetation information of the land surface. However, it is still challenging to simultaneously model the passive microwave observations at different frequencies (e.g. L-, C-, and X-band) due to the complex microwave emission and scattering mechanisms.

The zero[th]-order radiative transfer model, such as the widely used Tau-Omega model (Mo et al., 1982) adopted for the L-band microwave emission of the biosphere (L-MEB) model (Wigneron et al., 2007), SMAP baseline algorithm (O'Neill et al., 2020), and community microwave emission model (CMEM) (Holmes et al., 2008; de Rosnay et al., 2009), has often been used to simulate land surface emission. Among these, the L-MEB model and SMAP algorithm are specifically developed for L-band emission simulation, while the CMEM is designed to be able to simulate multi-frequency passive microwave emission at frequencies ranging from 1 to 20 GHz via implementing multiple parameterizations for several key variables such as surface roughness, VOD, soil permittivity and effective soil temperature. Specifically, the CMEM comprises parameterizations adopted by the L-MEB model and the Land Surface Microwave Emission Model (LSMEM) developed by Drusch et al. (2001), which can be equivalent to the L-MEB model when corresponding options are chosen. For instance, six parameterizations are adopted by the CMEM to estimate the impact of surface roughness on emission simulations, whereby several parameterizations such as the one developed by Wigneron et al. (2007) as also implemented by the L-MEB model is only applicable to the L-band, while other parameterizations such as the one proposed by Wegmüller and Mätzler (1999) is suitable for multiple frequencies.

In general, a number of optical properties must be parameterized prior to the application of abovementioned models, such as the VOD (τ), single scattering albedo (ω), and surface roughness coefficients. For example, VOD is parameterized as a function of leaf area index (LAI) in the L-MEB model (Wigneron et al., 2007), and it is related to the vegetation water content (VWC) multiplied by a coefficient (b) in the SMAP algorithm (O'Neill et al., 2020), whereby LAI and VWC are estimated using optical remote sensing data. As shown in previous studies (Jackson and Schmugge, 1991; Wigneron et al., 2004; Zhao et al., 2021), the values of b generally depend on vegetation morphology, wavelength and polarization. Four parameterizations are adopted by CMEM to compute

the VOD, including those proposed by Kirdyashev et al. (1979), Jackson and O'Neill (1990), Wegmüller et al. (1995), and Wigneron et al. (2007). On the other hand, ω is often parameterized via a land cover type-based look up table (LUT) and assumed to be independent on frequency in abovementioned models. It was shown that a large part of differences in simulating the brightness temperature (T_B^p) by abovementioned models can be attributed to the selection of different parameterizations of vegetation properties and/or surface roughness coefficients (de Rosnay et al., 2009; Montpetit et al., 2015; Chan et al., 2016; Zheng et al., 2018a, 2018b; de Rosnay et al., 2020). For example, de Rosnay et al. (2009) used 12 configurations of CMEM to simulate the C-band AMSR-E T_B^p observations and found that the Kirdyashev opacity model (Kirdyashev et al., 1979) is more suitable for the vegetation conditions in the West Africa. Zheng et al. (2018b, 2019) modified the parameterizations of vegetation opacity and surface roughness adopted by current SMAP algorithm to improve the L-band T_B^p simulations on the Tibetan Plateau. Recently, de Rosnay et al. (2020) adopted several parameterizations of the CMEM to simulate the L-band SMOS T_B^p observations and showed that the combination of surface roughness and vegetation opacity models developed by Wigneron et al. (2001, 2007) achieved the best match between SMOS observations and CMEM simulations. However, it should be noted that their researches mainly focused on simulating the T_B^p at a single frequency due to the fact that no parameterizations of model coefficients can reproduce well the satellite observations at different frequencies.

Besides the parametric models, several theoretical radiative transfer models have been developed and applied to simulate the multi-frequency microwave emission as well. These models are generally derived from either an analytical or numerical solution to the Maxwell's equations for the interaction of electric or magnetic fields in a weakly conducting medium (Kornelsen and Coulibaly, 2013). These models are more mathematically complicated and can be used in a wide variety of conditions with few a priori assumptions. For instance, a single-layer random discrete medium model was developed by Lang (1981) based on the distorted Born approximation, which was shown to be able to simulate well the airborne L-band radiometer observations over grasslands using realistic parameters for the canopy (Saatchi et al., 1994). Chauhan et al. (1994) also confirmed the suitability of this model to reasonably simulate the radiometric response of a corn canopy to a range of SM conditions. It should be noted that the distorted Born approximation is less suitable for multi-frequency studies with assumption of a weakly scattering medium. Based on an iterative solution of the radiative transfer equations, Karam (1997) developed a physical model to handle canopies of different geometric structure, which achieved well agreement with observations over corn and soybean canopies. Similarly, a fully polarimetric multiple scattering model was developed at the Tor Vergata University (shorten as TVG model) (Bracaglia et al., 1995; Ferrazzoli and Guerriero, 1996) based on the radiative transfer theory. The "discrete approach" is implemented by the TVG model to represent the quasi-real geometry of vegetation components, and different methods are adopted to approximately simulate the electromagnetic behaviour of each vegetation component at different frequencies. The matrix doubling algorithm is further implemented to account for the electromagnetic interactions among all the vegetation components that includes multiple scattering effects. The TVG model was also widely used to simulate satellite- and ground-based T_B^p observations at different frequencies over different land conditions (Della Vecchia et al., 2010; Guerriero et al., 2016; Vittucci et al., 2016).

Recently, validity of the TVG model was extensively tested for its application to the Tibetan Plateau mainly covered with grassland (Dente et al., 2014; Wang et al., 2018; Zheng et al., 2018b; Bai et al., 2019; Zheng et al., 2021a). The TVG model was firstly implemented by Dente et al. (2014) to simulate the C-band AMSR-E observations, which was further adopted to simulate the L-band Aquarius (Wang et al., 2018) and SMAP observations (Bai et al., 2019). It was shown that the TVG model can reproduce well the measured T_B^p signals of single frequency (i.e. C- or

L-band) via site-specific calibration. In addition, Zheng et al. (2018b) showed that the calibrated TVG model can be used to derive appropriate parameterization of VOD that addressed the overestimation of vegetation opacity on the Tibetan grassland using the SMAP algorithm. However, different sets of model parameter values were obtained for different frequencies in the abovementioned studies that focused on the same study area, and there is no attempt to simulate multi-frequency T_B^p observations using the TVG model up to now. It is still uncertain whether it is possible to simulate multi-frequency T_B^p observations using an identical physically-based model (e.g. TVG model) based on a single set of model parameters given the fact that these parameters may be only dependent on site condition instead of frequency. Therefore, an identical physically-based model with a single set of model parameters would be a breakthrough as it would allow for simultaneously simulating microwave emissions and estimating vegetation properties at multiple frequencies.

In addition to abovementioned parameterizations or estimations with the theoretical model, the VOD can be directly retrieved from the T_B^p observations at different frequencies (i.e. L-, C-, X-, and Ku-band) along with the retrieval of SM. For instance, both SM and VOD were retrieved by the SMOS-IC products using the multi-angular and dual-polarization SMOS T_B^p observations via inverting the L-MEB model (Fernandez-Moran et al., 2017). A new mono-angle retrieval algorithm (SMAP-IB) was developed to retrieve both SM and VOD from the dual-polarization SMAP T_B^p observations based on the L-MEB model as well (Li et al., 2022). A multi-temporal dual-channel retrieval algorithm (MT-DCA) was proposed by Konings et al. (2017) to simultaneously retrieve the SM, VOD, and ω from the dual-polarization SMAP enhanced T_B^p products. The land parameter retrieval model (LPRM) was adopted to retrieve SM and VOD based on the microwave polarization difference index (MPDI) using the multi-frequency AMSR-E observations (Liu et al., 2011). Recently, Li et al. (2021) have evaluated currently available multi-frequency VOD products and found that magnitudes of those VODs are comparable to each other at L-, C-, and X-band. On the contrary, Baur et al. (2019) estimated the relative canopy absorption and scattering at L-, C- and X-band and found that the seasonal amplitudes of VOD are higher for C- and X-band than for L-band, which exhibits frequency dependence. This phenomenon is consistent with the theory that the VOD is strongly dependent on the microwave wavelength with different penetration capability. It should be noted that different retrieval algorithms were implemented to retrieve the VOD from different satellites, which may also lead to the frequency independence of VOD as shown in Li et al. (2021), while the work of Baur et al. (2019) isolated effects only due to frequency. Therefore, further exploration of this phenomenon is thus imperative to better interpreting currently developed VOD products.

As shown above, most of current works mainly focused on simulating the satellite-based T_B^p observations at a single frequency either using the parametric or theoretical models, which prevent from exploring the benefit of using multi-frequency observations to detect complementary soil and vegetation information as planned by the CIMR mission. Since many needed vegetation (e.g. leaf dimension and water content) and soil (e.g. surface roughness) parameters are unknown at the satellite footprint, most often the theorical model was calibrated using different satellite observations at each individual frequency, leading to different parameter values for the same site that is against the fact that these parameters are only dependent on site condition instead of frequency. This further prevents from using the theorical model to investigate whether the VOD depends on frequency since the frequency dependence of parameter values was not isolated. Therefore, this study investigates the potential of using an identical physically-based model with a single set of model parameters to simultaneously simulate the satellite-based T_B^p observations and estimate the VOD at multiple frequencies (Fig. 1). For this investigation, the SMAP L-band (1.4 GHz) and AMSR2 C- (6.925 GHz) and X-band (10.7 GHz) observations are selected since these frequencies are often adopted to retrieve the SM and VOD and will also be implemented by the CIMR mission. The TVG model (Bracaglia et al., 1995; Ferrazzoli and Guerriero, 1996) is adopted to simulate the L-, C-, and X-band emissions over the Tibetan grassland ecosystems given the fact that in-depth works have been conducted over this region with the TVG model (Dente et al., 2014; Wang et al., 2018; Zheng et al., 2018b; Bai et al., 2019; Zheng et al., 2021a). Frequency-specific and multi-frequency calibration strategies are implemented to find the suitable set of model parameters (see Table 2 in Section 3.1) using the SMAP and AMSR2 T_B^p observations to isolate the impact of frequency on parameter values. On this basis, the calibrated TVG model is used to estimate VOD at the three frequencies that are further used to develop their parameterizations and validate currently available satellite-based VOD products. Moreover, the calibrated TVG model is adopted to investigate the impact of microwave frequency and observation angle on the emission simulations, as well as to develop parameterization of VOD at multi-frequency.

This paper is organized as follows. Section 2 introduces the study area and datasets of SMAP, AMSR2, and VOD products. Section 3 describes the TVG model and its calibration and validation strategies. The methods to estimate and parameterize the VOD values at the L-, C-, and X-band are also given in Section 3. Section 4 presents the multi-frequency emission simulation and the simulated emission component of soil and vegetation. The estimated multi-frequency VOD is further compared to currently developed microwave products in Section 4. In
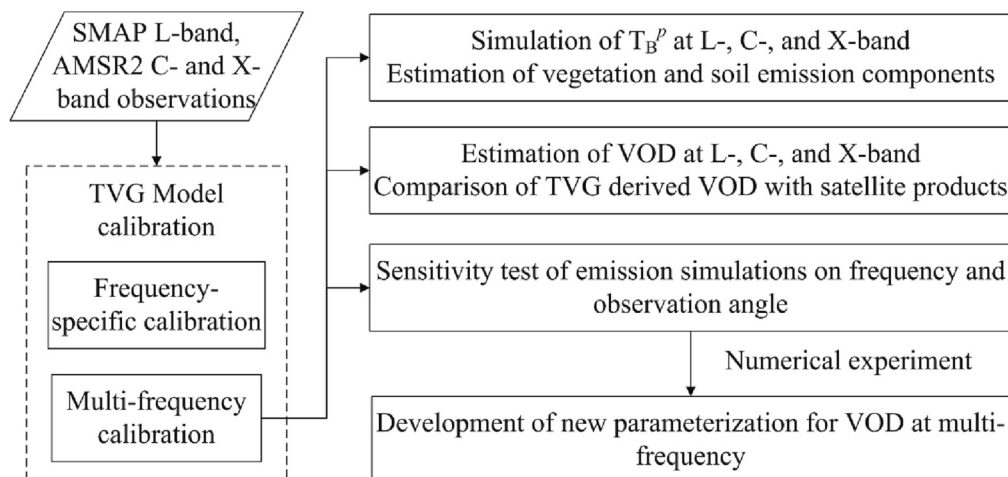

Fig. 1. Flowchart of this work.

addition, the effects of microwave frequency and observation angle on the emission process are discussed based on the calibrated TVG model. Further discussion on the TVG derived VOD and current satellite-based products is given in Section 5, and the development of parameterizations for VOD at multi-frequency is also discussed. The findings are summarized in Section 6.

2. Study area and datasets

This section introduces in order the study area and *in situ* SM and soil temperature (SMST) measurements, SMAP and AMSR2 T_B^p observations, MODIS LAI and satellite-based VOD products selected in this study. The *in situ* SMST measurements and MODIS LAI product are important input of the TVG model to characterize the soil permittivity and leaf coverage conditions (see Section 3.1). The SMAP and AMSR2 T_B^p observations are adopted to calibrate and validate the TVG model (see Section 3.2), and the satellite-based VOD retrievals are compared to the VOD values derived from the TVG simulations to investigate the dependence of VOD on frequency (see Section 4.3).

2.1. Maqu site and in situ measurements

The Maqu regional-scale SMST monitoring network is situated in the north-eastern edge of the Tibetan Plateau (33°30′-34°15′N, 101°38′-102°45′E), which covers an area of approximately 40 km by 80 km (Fig. 2a). The network was originally equipped with about 20 SMST profile measuring stations since July 2008 (Fig. 2b), and the SMST are generally measured at depths of 5, 10, 20, 40 and 80 cm every 15 min using the EC-TM and subsequent 5TM ECH$_2$O probes (Decagon Devices Inc., USA, now Meter group). The elevations range from 3.4 to 3.8 km above the sea level, and the dominant land cover is seasonal short grassland (Fig. 2c). The climate is characterized by dry and cold conditions in the cold season (from November to March) and rainy and warm conditions in the warm season (from April to October). The prevailing soil type is silt loam according to the measurements taken at 5 cm soil depth as reported in Dente et al. (2012a) and Zheng et al. (2015). As part of the Tibetan Plateau Observatory (Tibet-Obs) (Su et al., 2011), the Maqu network has been selected as one of the international validation sites for the calibration/validation of SMAP SM products (Colliander et al., 2017). A more detailed description of the Maqu network is available in Dente et al. (2012a).

Recently, Zhang et al. (2021) developed a continuous time series of spatially upscaled surface SM (0–5 cm) products based on the *in situ*

measurements taken from the Tibet-Obs for the period from May 2009 to May 2019. The upscaled product developed for the Maqu network is used in this study to represent the average surface SM conditions of the SMAP and AMSR2 grid cells, which was produced using only the sites (i. e. CST05, NST01 and NST03 shown in Fig. 2b) that provide the longest continuous measurements. Due to different imaging times of SMAP and AMSR2 orbits, the *in situ* SMST measurements are used to represent the soil conditions corresponding to the ascending and descending over-passes of SMAP (i.e. 6:00 PM and 6:00 AM at local time) and AMSR2 (i.e. 1:30 PM and 1:30 AM), respectively. Previous studies have shown that the soil is subject to strong freezing and thawing during the cold season (Zheng et al., 2017a), and the contribution of vegetation to the land microwave emission is found to be negligible (Zheng et al., 2021a). Therefore, only the *in situ* SMST measurements collected during the warm seasons (from April to October) are used as inputs to simulate T_B^p and estimate vegetation properties (e.g. VOD) by the TVG model.

2.2. SMAP product

With the aim of providing global measurements of SM and monitoring the landscape freeze/thaw condition, the NASA's SMAP satellite was launched in January 2015 (Entekhabi et al., 2010). It is equipped with an L-band radar (1.26 GHz) and radiometer (1.41 GHz). Due to hardware malfunction, the radar stopped working on 7 July 2015. The SMAP observed the Earth from a sun-synchronous, near-circular orbit with the ascending node at 6:00 PM and descending node at 6:00 AM at local time. The radiometer measures T_B^p at a constant incidence angle of 40° with a 2–3 day revisit time. Until now, the SMAP mission has provided five years products of surface SM (O'Neill et al., 2020), freeze/thaw conditions (Xu et al., 2020) and root zone SM (Reichle et al., 2020).

In this paper, the SMAP Level-3 global daily radiometer SM product (version 7, SPL3SMP) with a grid resolution of 36 km is used. The reason for selecting this data version is that it keeps consistent with the version of VOD products used in this study (see Section 2.5). The temporal coverage of this product ranges from April 1, 2015 to October 31, 2018 that is consistent with the availability of *in situ* SMST measurements (see Section 2.1). The SPL3SMP includes T_B^p, surface SM, VOD, ω, and other auxiliary data. The SPL3SMP data can be downloaded from the National Snow and Ice Data Center (https://nsidc.org/data/smap/smap-data.html). In this study, three SMAP grid cells covering the three representative monitoring sites (see Section 2.1) are selected and averaged to represent the SMAP observations of the study area, and only the data produced in the monsoon season (from April to October) for both AM
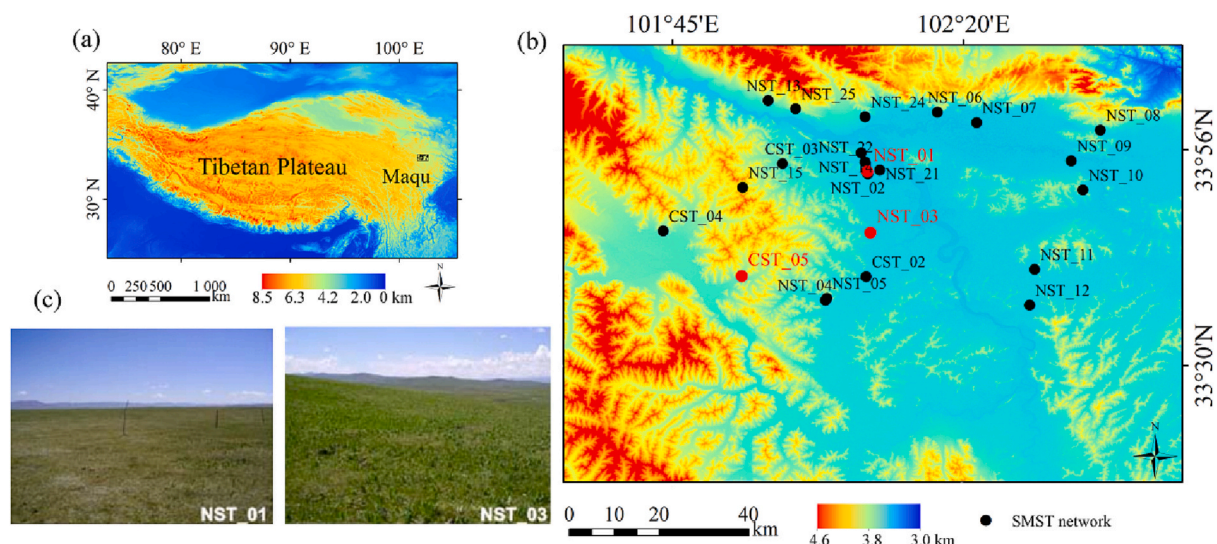

Fig. 2. Geographical location of the Maqu SMST monitoring network.

and PM overpasses are used.

2.3. AMSR2 product

The AMSR2 sensor onboard the GCOM-W1 satellite measures microwave emission from the land surface and atmosphere of the Earth (Imaoka et al., 2010). The GCOM-W1 satellite observes the Earth from a sun-synchronous sub-recurrent orbit with ascending node at 1:30 PM and descending node at 1:30 AM, which covers 99% of the Earth every 2 days. The AMSR2 is a multi-frequency microwave radiometer that observes microwave emission at frequencies of 6.925, 7.3, 10.65, 18.7, 23.8, 36.5, and 89.0 GHz and incidence angle of 55°. Since 2012, the AMSR2 mission has provided T_B^p datasets as well as geophysical parameters including surface SM (https://gcom-w1.jaxa.jp/).

In this paper, the AMSR2 Level-3 dual-frequency (6.925 and 10.65 GHz) observations with a grid resolution of 25 km are used, which are obtained from the GCOM-W1 data providing service (https://gcom-w1.jaxa.jp/). The reason for choosing this data version is to match the subsequent VOD products selected in Section 2.5. In this study, the temporal coverage is set from April 2015 to October 2018 consistent with the SMAP data. Two AMSR2 grid cells covering the three representative monitoring sites (see Section 2.1) are selected and averaged as well, and also only the data produced in the monsoon season during both AM and PM overpasses are used. Using the similar criteria applied in previous studies (de Nijs et al., 2015), the T_B^p data is filtered to avoid too high or too low values caused by the radio frequency interference.

2.4. MODIS LAI product

LAI is an important input parameter for simulating vegetation scattering using the TVG model (see Section 3). The Terra+Aqua MODIS LAI 4-day L4 global products spanning from April 2015 to October 2018 with spatial resolution of 500 m are used in this study, which are downloaded from EARTHDATA (https://earthdata.nasa.gov). Preprocessing of the LAI product includes projection, resampling, smoothing, and interpolation. The original SIN Grid is firstly re-projected to a geographic projection (datum: WGS84), which is then resampled from 500 m to 36 km and 25 km to be consistent with the spatial resolution of SMAP and AMSR2, respectively. The harmonic analysis of the time series (HANTS) filter (Verhoef et al., 1996) is further used to smooth the MODIS LAI to remove the cloud contamination. Later on, the smoothed LAI is interpolated with the cubic spline interpolation technique to compute the LAI values for the acquisition dates of SMAP and AMSR2, respectively. In this study, the LAI is used as an input of TVG model to characterize the vegetation status.

2.5. VOD products

Recently developed satellite-based VOD products will be compared to the estimated VOD results derived from the TVG simulations to validate their performance in this study. Table 1 lists the VOD datasets used in this study, which are mainly obtained from SMAP, SMOS, and AMSR2 observations.

The SMAP products use the single-channel algorithm (SCA) at vertical or horizontal polarization and dual-channel algorithm (DCA) to retrieved SM from T_B^p observations (O'Neill et al., 2020). For the SCA, the VOD is linearly related to the VWC that is a function of NDVI (Chan et al., 2016). For the DCA, the VOD is retrieved along with the SM (O'Neill et al., 2020). The MT-DCA simultaneously retrieves SM, VOD, and ω from dual-polarization SMAP Backus-Gilbert enhanced T_B^p products using a moving window to combine retrievals from two consecutive overpasses (Konings et al., 2017), during which the VOD is assumed to be constant. The SMOS-L3 is based on a multi-orbit algorithm to retrieve SM and VOD (Al Bitar et al., 2017), which uses ECMWF SM in the retrievals and uses LAI to initialize and constrain VOD retrievals (Al Bitar et al., 2017; Wigneron et al., 2021). The SMOS-IC retrieves SM and VOD using the multi-angle and dual-polarization SMOS-L3 T_B^p products by means of inverting the L-MEB model (Fernandez-Moran et al., 2017; Wigneron et al., 2021), which is independent of any auxiliary variables.

The LPRM algorithm simultaneously retrieves SM and VOD (Liu et al., 2011) based on the microwave polarization difference index (MPDI) with the use of an analytical retrieval methodology (Meesters et al., 2005). The C- and X-band VOD produced by the LPRM V5 (Owe et al., 2008) is used in this study due to the fact that the latest version (V6) is not publicly available (van der Schalie et al., 2017). The vegetation optical depth climate archive (VODCA) combines the VOD retrievals derived from multiple sensors at C-, X-, and Ku-band using the LPRM algorithm (Liu et al., 2011) into a single long-term VOD dataset (Moesinger et al., 2020). A cumulative distribution function is adopted by VODCA to scale multi-source VOD retrievals to the one of AMSR-E VOD to eliminate the biases between the VOD values retrieved from different sensors. In this study, only C- and X-band VODCA datasets retrieved from AMSR2 are used. The global land parameter data record (LPDR) is generated from calibrated, multi-frequency T_B^p observations of AMSR-E and AMSR2 (Du et al., 2017), whereby VOD is obtained by inverting the land-water microwave emissivity slope index (Du et al., 2017). The LPDR version 2 VOD used in this study is retrieved from AMSR2 (10.65 GHz).

3. Methods

3.1. TVG model

The TVG model (Bracaglia et al., 1995; Ferrazzoli and Guerriero, 1996) is used in this study to simulate the multi-frequency emission because its performance was extensively validated in the Maqu area (Dente et al., 2014; Wang et al., 2018; Zheng et al., 2018b; Bai et al., 2019; Zheng et al., 2021a). As in previous studies (Dente et al., 2014; Zheng et al., 2021a), the grass is represented by thin dielectric discs with random distribution of orientation, whereby the scattering coefficient of the dielectric discs is computed using the Rayleigh-Gans approximation (Eom and Fung, 1984) and physical optics approximation (LeVine et al.,

Table 1
Characteristics of the VOD products used in this study.

Product	Sensor	Frequency	Spatial Resolution	Reference	Data Link
SMAP-SCA SMAP-DCA	SMAP		36 km	(O'Neill et al., 2020)	https://nsidc.org/data/SPL3SMP/versions/7
MT-DCA			9 km	(Konings et al., 2017)	http://afeldman.mit.edu/mt-dca-data
SMOS-L3		1.4 GHz (L-band)		(Al Bitar et al., 2017)	https://www.catds.fr/Products/Products-access
SMOS-IC	SMOS			(Fernandez-Moran et al., 2017; Wigneron et al., 2021)	https://ib.remote-sensing.inrae.fr/
VODCA (Version 1)	AMSR2	6.925 GHz (C-band),	25 km	(Moesinger et al., 2020)	https://zenodo.org/record/2575599
LPRM (Version 5)		10.65 GHz (X-band)		(Liu et al., 2011)	https://geo.vu.nl/~jeur/lprm/index.html
LPDR (Version 2)		10.65 GHz (X-band)		(Du et al., 2017)	http://files.ntsg.umt.edu/data/LPDR_v2/

1983) for frequency below and above 5 GHz, respectively. Thickness, radius, and permittivity of the disc and leaf coverage are necessary to compute the scattering and absorption coefficients of grass. The LAI derived from the MODIS product (see Section 2.4) is used to describe the leaf coverage. The vegetation mixing model developed by Mätzler (1994) is adopted to compute the vegetation permittivity with gravimetric moisture of the disc as input. The soil surface is described as a homogeneous half-space with a rough interface that is simulated by the integral equation model (IEM) (Fung, 1994). The soil permittivity, root mean square (RMS) height, and correlation length of surface roughness are required to parameterize the IEM model. The soil permittivity is estimated with the four-phase dielectric mixing model developed by Birchak et al. (1974) that has been extensively validated (Schwank et al., 2004; Zheng et al., 2017b; Zheng et al., 2021a). The upscaled surface SM at 5 cm developed by Zhang et al. (2021) (see Section 2.1) is used to estimate the soil permittivity for different frequencies (i.e. L-, C-, and X-band). Here we assume soil moisture to be vertically uniform within the emission depth at L-, C-, and X-band as in Baur et al. (2019). As shown in Baur et al. (2019), the near-hydrostatic profile is the most likely state of moisture in the soil column during the overpass of SMAP and AMSR2 satellites. The presence of litter is also included in the soil scattering contribution, which is modeled as a mixture of air and dielectric material overlaying the soil. Litter moisture content and biomass are necessary to compute the scattering matrices for the litter. The matrix doubling method (Eom and Fung, 1984) is applied twice: once to compute the total vegetation contribution and once to obtain the total contribution by combining vegetation contribution with that of the soil-litter medium. The emissivity (e) is computed by applying the Kirchoff's energy conservation law, and T_B^p is obtained as the product of e and soil effective temperature that is computed using the theoretical formulation developed by Choudhury et al. (1982) with the profile SMST measurements as input. A more detailed description of the TVG model can be found in Dente et al. (2014) and Zheng et al. (2017b).

The needed input parameters for the TVG model to simulate the SMAP and AMSR2 T_B^p observations are summarized in Table 2, which can be categorized into five types related to satellite sensor configurations, and properties of soil surface, canopy, leaves and litter. Specifically, the TVG model is implemented to simulate the T_B^p observations at L- (1.41 GHz), C- (6.925 GHz), and X-band (10.65 GHz) with incidence angles of 40°, 55°, and 55°, respectively. The SM and LAI are obtained from the upscaled SM dataset (see Section 2.1) and MODIS LAI product (see Section 2.4) to characterize soil permittivity and leaf coverage conditions. Supported by the results of sensitivity analysis conducted by previous studies for the Maqu area (Dente et al., 2014; Wang et al., 2018; Bai et al., 2019), six relatively sensitive model parameters for emission simulation are chosen to optimize the TVG model using the SMAP and AMSR2 T_B^p observations, namely the ratio of litter moisture content to SM (Plitter), litter biomass (Blitter), disc radius (add), plant moisture

content (vgwc), RMS height (sig), and correlation length (lz). Other relatively insensitive model parameters are derived from Dente et al. (2014), including autocorrelation function of surface roughness (ACF), disc thickness (ldd) and angular distribution as listed in Table 2. These parameters are assumed to be constant for the entire warm seasons except the SM and LAI. Detailed description of the optimization methods for the six selected sensitive model parameters is given in following section. The outputs of the TVG model include the simulated total T_B^p at the vertical (T_B^V) and horizontal (T_B^H) polarizations, vegetation and soil emission components, and vegetation transmissivity for the three selected frequencies.

3.2. Model calibration and validation

In this study, the TVG model is calibrated using the SMAP and AMSR2 T_B^p observations to obtain values for the six selected unknown model parameters as listed in Table 2, i.e. the ratio of litter moisture content to SM (Plitter), litter biomass (Blitter), disc radius (add), plant moisture content (vgwc), RMS height (sig), and correlation length (lz). Two different calibration strategies are implemented. In the first calibration case (called as "Sim1"), the six model parameters are optimized to match the TVG simulation with either the L-band SMAP or the C−/X-band AMSR2 observations acquired at AM and PM overpasses, respectively. For this case, three sets of calibrated model parameter values can be obtained for the three frequencies, and the corresponding cost functions are listed as follows,

$$S_L = \frac{RMSE\left(T_{B,AM}^H\right)}{\Delta T_{B,AM,L}^H} + \frac{RMSE\left(T_{B,AM}^V\right)}{\Delta T_{B,AM,L}^V} + \frac{RMSE\left(T_{B,PM}^H\right)}{\Delta T_{B,PM,L}^H} + \frac{RMSE\left(T_{B,PM}^V\right)}{\Delta T_{B,PM,L}^V}$$

(1a)

$$S_C = \frac{RMSE\left(T_{B,AM}^H\right)}{\Delta T_{B,AM,C}^H} + \frac{RMSE\left(T_{B,AM}^V\right)}{\Delta T_{B,AM,C}^V} + \frac{RMSE\left(T_{B,PM}^H\right)}{\Delta T_{B,PM,C}^H} + \frac{RMSE\left(T_{B,PM}^V\right)}{\Delta T_{B,PM,C}^V}$$

(1b)

$$S_X = \frac{RMSE\left(T_{B,AM}^H\right)}{\Delta T_{B,AM,X}^H} + \frac{RMSE\left(T_{B,AM}^V\right)}{\Delta T_{B,AM,X}^V} + \frac{RMSE\left(T_{B,PM}^H\right)}{\Delta T_{B,PM,X}^H} + \frac{RMSE\left(T_{B,PM}^V\right)}{\Delta T_{B,PM,X}^V}$$

(1c)

where RMSE(.) stands for the root mean square error computed between TVG simulations and satellite observations, and Δ indicates the standard deviation of satellite observations selected for model calibration. It should be noted that the weights of polarization (i.e. T_B^H and T_B^V) and overpass time (i.e. AM and PM) are considered equal to obtain the optimized parameters in the cost function.

In the second calibration case (called as "Sim2"), the L-band SMAP and the C- and X-band AMSR2 T_B^p observations are simultaneously used

Table 2
Input parameters for the TVG model to simulate the SMAP and AMSR2 observations.

Input	Definition	Label	Values/Ranges	
Sensor	frequency (GHz)	f	1.41 (SMAP-L); 6.925 (AMSR2-C); 10.65 (AMSR2-X)	
	observation angle (°)	θ	40 (SMAP); 55 (AMSR2)	
	soil moisture (m³/m³)	mv	Upscaled surface SM based on *in situ* measurements	Zhang et al. (2021)
Soil surface	RMS height (cm)	sig	[0.1:0.1:2.0]*	
	correlation length (cm)	lz	[1:2:19]*	**Calibration**
	autocorrelation function	ACF	exponential	Dente et al. (2014)
Canopy	LAI (cm²/cm²)	lai	MODIS LAI product	
	disc radius (cm)	add	[1.0:0.1:1.6]*	**Calibration**
Leaves	disc thickness (cm)	ldd	0.02	
	disc angular distribution	–	random	Dente et al. (2014)
	plant moisture content (g/g)	vgwc	[0.4:0.1:0.9]*	
Litter	litter moisture content (m³/m³)	gmoist	gmoist = Plitter×mv Plitter = [0.5:0.5:2.0]*	**Calibration**
	litter biomass (g/cm²)	Blitter	[0.00:0.02:0.10]*	

* x1: x2: x3: calibrated values change from x1 to x3 with interval of x2.

to optimize the six model parameters. In this case, only a single set of calibrated model parameter values is obtained for the three-frequency T_B^p simulations, and the corresponding cost function is listed as follows,

$$S_{ALL} = S_L + S_C + S_X \tag{2}$$

It should be noted that the weights of polarization, overpass time and frequency (i.e. L-, C-, and X-band) are considered equal to obtain the optimized parameters in the cost function.

The first calibration strategy (i.e. Sim1) was extensively adopted by previous studies (Dente et al., 2014; Wang et al., 2018; Bai et al., 2019) to match the TVG simulation with different satellite observations at different frequencies. Although this strategy generally leads to different sets of parameter values for the same study area, it may produce the best match between the TVG simulation and satellite observations at each individual frequency. On the other hand, the second calibration strategy (i.e. Sim2) can avoid the impact of frequency on parameter values, allowing the TVG model to simultaneously simulate the satellite observations and estimate the VOD at multiple frequencies using a single set of parameter values. As such, the dependence of VOD on frequency can be elaborated. In addition, it may imply that the selected model parameters are not frequency dependent if the performance of Sim2 is comparable to the Sim1.

In both calibration cases, the previous two years' data of SMAP and AMSR2 observations (i.e. 2015 and 2016) are used for model calibration and the remaining two years' data (i.e. 2017 and 2018) are used for model validation. A look up table (LUT) method is applied to find a set of input parameters that can minimize above cost functions using the method proposed by Bai et al. (2019). Specifically, the range for the *Plitter* value is set between 0.5 and 2.0 with interval of 0.5, and the *Blitter* value ranges from 0 to 0.1 g/cm² with increment of 0.02 g/cm². The value of *vgwc* changes from 0.4 to 0.9 g/g with interval of 0.1 g/g, and the *add* value ranges from 1.0 to 1.6 cm with interval of 0.1 cm. The *sig* value ranges from 0.1 to 2.0 cm with interval of 0.1 cm, and the value of *lz* changes from 1 to 19 cm with increment of 2 cm. There are about 201,600 simulations based on the parameter combinations, i.e. 4 (*Plitter*) × 6 (*Blitter*) × 7 (*add*) × 6 (*vgwc*) × 20 (*sig*) × 10 (*lz*) =201,600. As in Bai et al. (2019), the values of the cost function are computed by executing the iteration of all possible combinations during the calibration period, and the optimized parameters are obtained via searching among all simulations to find the global minimum of the cost function.

3.3. Estimation and parameterization of VOD

As in previous studies (Ferrazzoli et al., 2002; Zheng et al., 2018b), VOD can be estimated from the simulated transmissivity (γ^p) of the vegetation canopy by the TVG model as,

$$VOD^p = -ln(\gamma^p) \times cos\theta \tag{3}$$

where *p* stands for the polarization (*p* = H, V), and θ is the incidence (observation) angle of satellite observations.

VOD derived from the TVG simulations are further compared to recently developed VOD products (see Section 2.5), and are also used to develop corresponding parameterizations as in Zheng et al. (2018b),

$$VOD^p = b \times LAI \tag{4}$$

where *b* represents the coefficients depending on microwave frequency. The selection of LAI for parameterizing VOD mainly follows the work of Jackson and O'Neill (1990) and Wigneron et al. (2007), whereby VOD is related to VWC that is described as a function of LAI.

4. Results

4.1. Multi-frequency emission simulation

Table 3 lists the optimized parameters of the TVG model in Sim1 (see Section 3.2) by minimizing the cost functions in Eqs. (1a)-(1c) for the L-band SMAP, and C- and X-band AMSR2 T_B^p observations, respectively. In general, the optimized parameter values are different for the three frequencies in Sim1, and the values are closer to each other for the C- and X-band AMSR2 observations. The obtained parameter values for the C-band are also comparable to those reported by Dente et al. (2014) using C-band AMSR-E observations for the 2009 monsoon season (see Table 3 in Dente et al. (2014)). The optimized parameters obtained in Sim2 by minimizing the cost function in Eq. (2) for all three frequencies are also given in Table 3, which are different with those of Sim1 as well. Nevertheless, it can be found that the values of litter parameters (i.e. *Plitter* and *Blitter*), disc radius (*add*) and correlation length (*lz*) are comparable to each other between different frequencies and calibration strategies, while the values for vegetation water content (*vgwc*) and RMS height (*sig*) show large differences. The possible reason may ascribe to different penetration capability at different frequencies. At L-band, the observed total scattering mainly comes from the soil surface, which thus leads to a relatively larger RMS height. At C- and X-band, the vegetation scattering contribution is far beyond the soil scattering component, leading to relatively larger vegetation water content.

Tables 4 and 5 show the error statistics, i.e. bias, RMSE, unbiased RMSE (ubRMSE), and correlation coefficient (R), computed between the T_B^p observations and simulations produced by the Sim1 and Sim2 during both AM and PM overpasses for the calibration and validation periods, respectively. As for the calibration results of Sim1, the calibrated TVG model shows good performance in simulating the SMAP and AMSR2 T_B^p observations based on frequency-specific calibration. In general, the TVG simulations better capture the high frequency AMSR2 observations than the low frequency SMAP observations during the AM overpass as indicated by lower bias and RMSE values, while the performance is comparable to each other during the PM overpass. The simulations better capture the SMAP observations at PM than those at AM as indicated by lower bias and RMSE values and higher R value. On the contrary, the Sim1 better captures the AMSR2 observations at AM than those at PM especially for the X-band as indicated by lower bias and RMSE values. However, it should be noted that the R values for the PM are generally higher than those of AM for both C- and X-band. For the three frequencies, the T_B^V observations are generally better simulated than the T_B^H as indicated by lower RMSE values. For the validation period, the magnitudes of bias and RMSE of Sim1 are comparable to those of the calibration period, indicating good performance and transferability of the calibrated TVG model. The TVG simulations also capture better the T_B^V observations for the three frequencies as in the calibration period.

In comparison to Sim1, Sim2 attempts to find an identical set of input

Table 3
Optimized parameter values for the TVG model using the SMAP and AMSR2 observations based on two calibration strategies.

Simulation	Satellite data	Optimized parameters					
		Plitter (−)	*Blitter* (g/cm²)	*vgwc* (g/g)	*add* (cm)	*sig* (cm)	*lz* (cm)
Sim1	SMAP-L	1.5	0.02	0.5	1.6	1.7	3
	AMSR2-C	2	0.04	0.9	1.6	0.8	3
	AMSR2-X	2	0.04	0.7	1.5	0.6	1
Sim2	SMAP+AMSR2	2	0.02	0.7	1.6	1.9	5

Table 4
Error statistics for the TVG model simulations of T_B^H during calibration and validation periods.

Satellite	Simulation	Calibration				Validation			
		Bias (K)	RMSE (K)	ubRMSE (K)	R	Bias (K)	RMSE (K)	ubRMSE (K)	R
AM									
SMAP-L	Sim1	−5.04	10.82	9.58	0.76	−1.95	10.13	9.94	0.81
	Sim2	−3.16	10.47	9.98	0.75	−0.39	9.92	9.91	0.80
AMSR2-C	Sim1	0.51	7.22	7.20	0.78	2.21	7.10	6.75	0.80
	Sim2	1.80	8.01	7.81	0.78	3.39	7.92	7.16	0.80
AMSR2-X	Sim1	1.01	4.01	3.88	0.74	1.84	4.60	4.22	0.78
	Sim2	0.05	4.28	4.28	0.72	1.03	4.64	4.53	0.76
PM									
SMAP-L	Sim1	2.57	7.45	6.95	0.91	6.21	10.43	8.37	0.86
	Sim2	4.90	8.37	6.78	0.91	7.96	11.70	8.57	0.86
AMSR2-C	Sim1	0.45	7.20	7.19	0.87	5.41	9.93	8.33	0.84
	Sim2	1.79	7.28	7.06	0.87	6.60	10.49	8.15	0.84
AMSR2-X	Sim1	−3.47	7.79	6.97	0.86	0.73	7.88	7.85	0.82
	Sim2	−4.45	8.11	6.79	0.84	−0.14	7.69	7.69	0.81

Table 5
Error statistics for the TVG model simulations of T_B^V during calibration and validation periods.

Satellite	Simulation	Calibration				Validation			
		bias (K)	RMSE (K)	ubRMSE (K)	R	bias (K)	RMSE (K)	ubRMSE (K)	R
AM									
SMAP-L	Sim1	−3.47	8.13	7.35	0.77	−0.92	7.17	7.11	0.83
	Sim2	−4.29	9.12	8.04	0.76	−2.13	7.65	7.34	0.83
AMSR2-C	Sim1	1.99	3.40	2.76	0.78	2.25	3.65	2.87	0.85
	Sim2	1.79	4.60	4.23	0.77	2.23	4.39	3.79	0.84
AMSR2-X	Sim1	0.60	2.42	2.34	0.70	0.75	2.53	2.42	0.81
	Sim2	1.36	2.76	2.40	0.65	1.49	2.98	2.58	0.79
PM									
SMAP-L	Sim1	1.35	4.68	4.48	0.93	4.30	7.45	6.08	0.89
	Sim2	0.70	5.14	5.09	0.93	3.17	7.41	6.70	0.89
AMSR2-C	Sim1	−4.14	6.28	4.72	0.86	−0.64	5.03	4.99	0.85
	Sim2	−4.27	6.03	4.26	0.84	−0.65	4.57	4.53	0.85
AMSR2-X	Sim1	−7.67	8.85	4.42	0.82	−4.30	6.25	4.54	0.83
	Sim2	−6.89	8.35	4.72	0.79	−3.54	5.99	4.84	0.80

parameters to simultaneously capture well both the SMAP and AMSR2 observations at different frequencies. Interestingly, the performances of Sim2 are comparable to Sim1 for both the calibration and validation periods. Specifically, the *R* values obtained for Sim1 and Sim2 are close to each other for both polarizations especially at L- and C-band during both calibration and validation periods. Regarding to RMSE and ubRMSE, the values obtained for Sim1 and Sim2 are also comparable to each other, with maximum RMSE and ubRMSE differences noted between Sim1 and Sim2 are less than 1.20 and 1.50 K. These statistical indicators demonstrate the possibility to simulate multi-frequency T_B^p observations using an identical physically-based model (i.e. TVG model) based on a single set of model parameters. Similar to Sim1, the T_B^V observations are also better captured by Sim2 for the three frequencies.

Figs. 3a-3c show respectively the time series of SMAP L-band and AMSR2 C- and X-band T_B^p observations and simulations produced by both Sim1 and Sim2 during the PM overpass for both calibration and validation periods. The results of AM are similar to those of PM, and thus only the results of PM are shown as examples. The gap noted for the simulations in 2016 is caused by the absence of *in situ* SM measurements. The T_B^p observations at both polarizations generally increase with increasing frequency, and the increments are relatively larger from L- (i.e. 1.4 GHz) to C-band (i.e. 6.9 GHz) and smaller from C- to X-band (i.e. 10.65 GHz). In addition, the T_B^p observations also increase from spring to the middle of summer and then decline towards the winter due to growth and senescence of vegetation. The plots illustrate that the calibrated TVG model captures well the seasonal dynamics and magnitudes of SMAP and AMSR2 measured T_B^H and T_B^V especially at L- and C-band during both the calibration and validation periods. Also, variations

observed over short time scales are well captured by the TVG simulations such as the peak of vegetation growth between July 29 and August 12 in 2017 as shown in Fig. 3. Fig. 3 also shows that the simulations produced by Sim1 and Sim2 are comparable to each other for the three frequencies at both polarizations, confirming the suitability to use the TVG model based on a single set of model parameters to simulate satellite-based T_B^p observations at different frequencies. This also allows using the TVG model to estimate multi-frequency vegetation properties and investigate the dependence of VOD on frequency after isolating the impact of frequency on parameter values. Therefore, the Sim2 simulations are used for the further analysis in the following sections.

4.2. Estimation of the emission components and VOD

Fig. 4 shows the emission components produced by the Sim2 simulations for the three frequency at PM during the whole study period. As expected, the component of vegetation increases with the growth of vegetation and decreases with the senescence of vegetation for the three frequencies, while the soil component with consideration of vegetation attenuation shows an opposite change trend especially at the C- and X-band. For instance, the vegetation component generally reaches its maximum while the soil component declines to its minimum at the peak of vegetation growth especially for the C- and X-band. In general, the value of vegetation component at horizontal polatization is higher than at the vertical polarization, while the soil component shows opposite polarization dependence.

Due to different penetration capability, the amplitudes of the simulated vegetation and soil components are different for the three selected
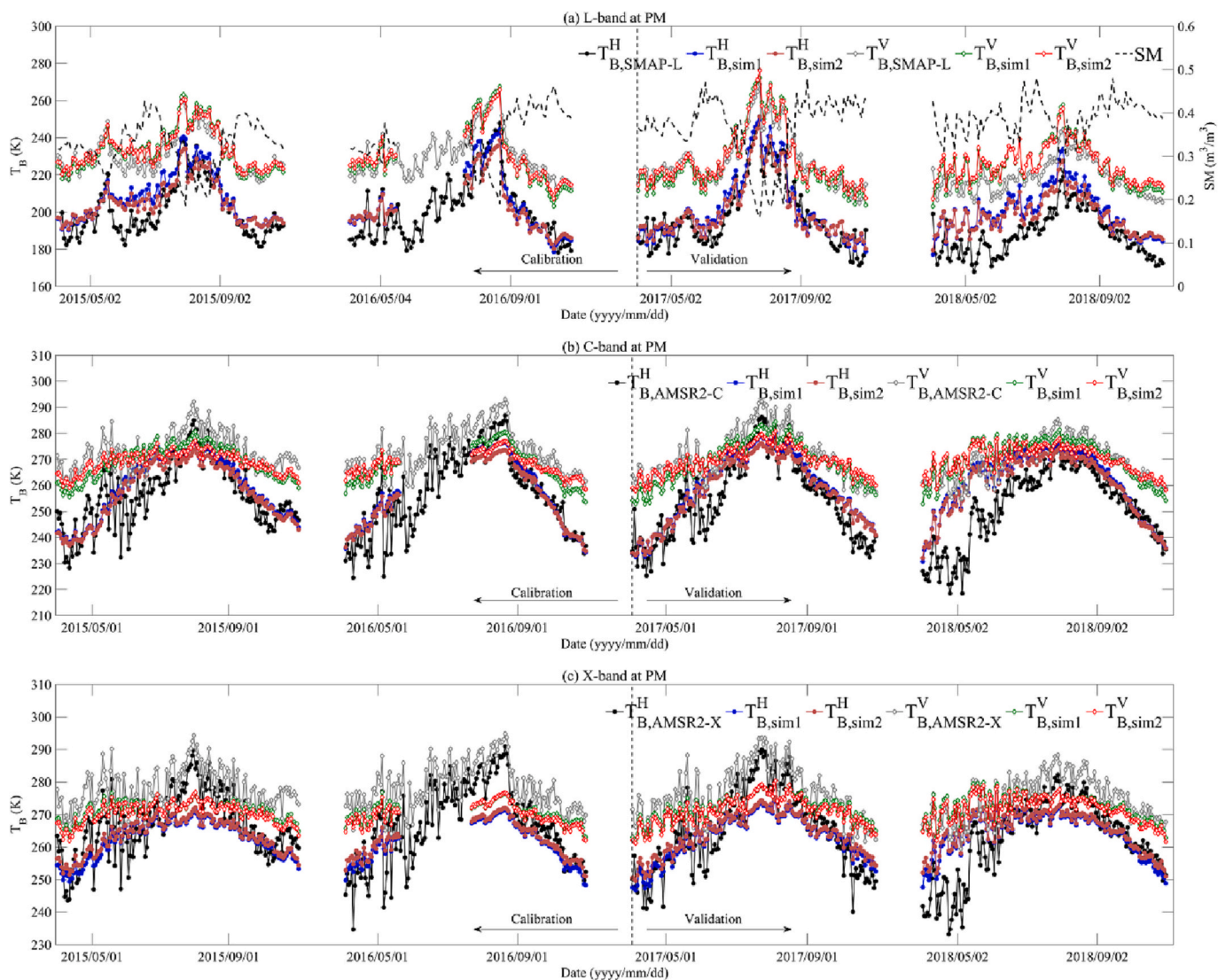
Fig. 3. Time series of (a) SMAP L-band, and AMSR2 (b) C- and (c) X-band T_B^H and T_B^V observations and simulations at PM produced by the Sim1 and Sim2 during both calibration (2015–2016) and validation (2017–2018) periods separated by a vertical dotted line.

frequencies. At L-band (1.4 GHz), the vegetation component is very small (≤ 50 K) even at the peak of vegetation growth, and the soil component dominates the total emission during the whole study period. A similar finding has also been reported by previous studies (Wang et al., 2018; Zheng et al., 2018b; Zheng et al., 2021a). For the C- (6.9 GHz) and X-band (10.7 GHz), the vegetation component is much larger and dominates the total emission during the vegetation growth period from early June to the middle of October, while the soil component dominates in the remaining period. These results confirm the stronger capabilites of low frequency (e.g. L-band) in detecting SM, while the higher frequency (e.g. C- and X-band) are more affected by the vegetation coverage especially during the growth period. In summary, the big differences noted between the simulated vegetation and soil contributions at L-band and those for C- and X-band are mainly affected by the penetration capability of different frequencies, which is further elaborated in Section 4.4.

Fig. 5 shows the estimated VOD using Eq. (3) based on the Sim2 simulations for the three frequency at PM during the whole study period. The values of VOD generally increase with increasing frequency, and they are much smaller at L-band than at C- and X-band. This is more than expected for L-band for SM monitoring and may have contributed to large improvement in the SM products going from C- to L-band. In

addition, the seasonal amplitudes of VOD also increase with increasing frequency from L- to X-band with C- and X-band being very similar, and similar finding was also reported in Baur et al. (2019). These results are in line with the theoretical principle that the vegetation contribution increases with increasing frequency due to increasing extinction effect, leading to larger VOD values at higher frequency than those at lower frequencies. In addition, the VOD value at the horizontal polarization is larger than at the vertical polarization especially at peak biomass due to the fact that the simulated vegetation component is also larger at the horizontal polarization (Fig. 4), and the difference is much smaller at L-band. This supports the assumption of polarization independence for the VOD in the SMAP and SMOS algorithms for grassland. The estimated VODs for the three frequencies generally follow the dynamics of vegetation growth, which can be linearly correlated to the LAI variations using Eq. (4) as in Zheng et al. (2018b), whereby the coefficient *b* is fitted from the estimated VOD and MODIS LAI product. The obtained *b* values generally increase with increasing frequency (Fig. 5), and the values for the C- and X-band are more than ten times larger than the one of L-band, i.e. 0.024, 0.238 and 0.328 for the L-, C- and X-band. The high correlation found between the TVG derived VODs and the LAI for all three frequencies is mainly due to the vegetation water content of grassland is primarily determined by the amount of foliage in the
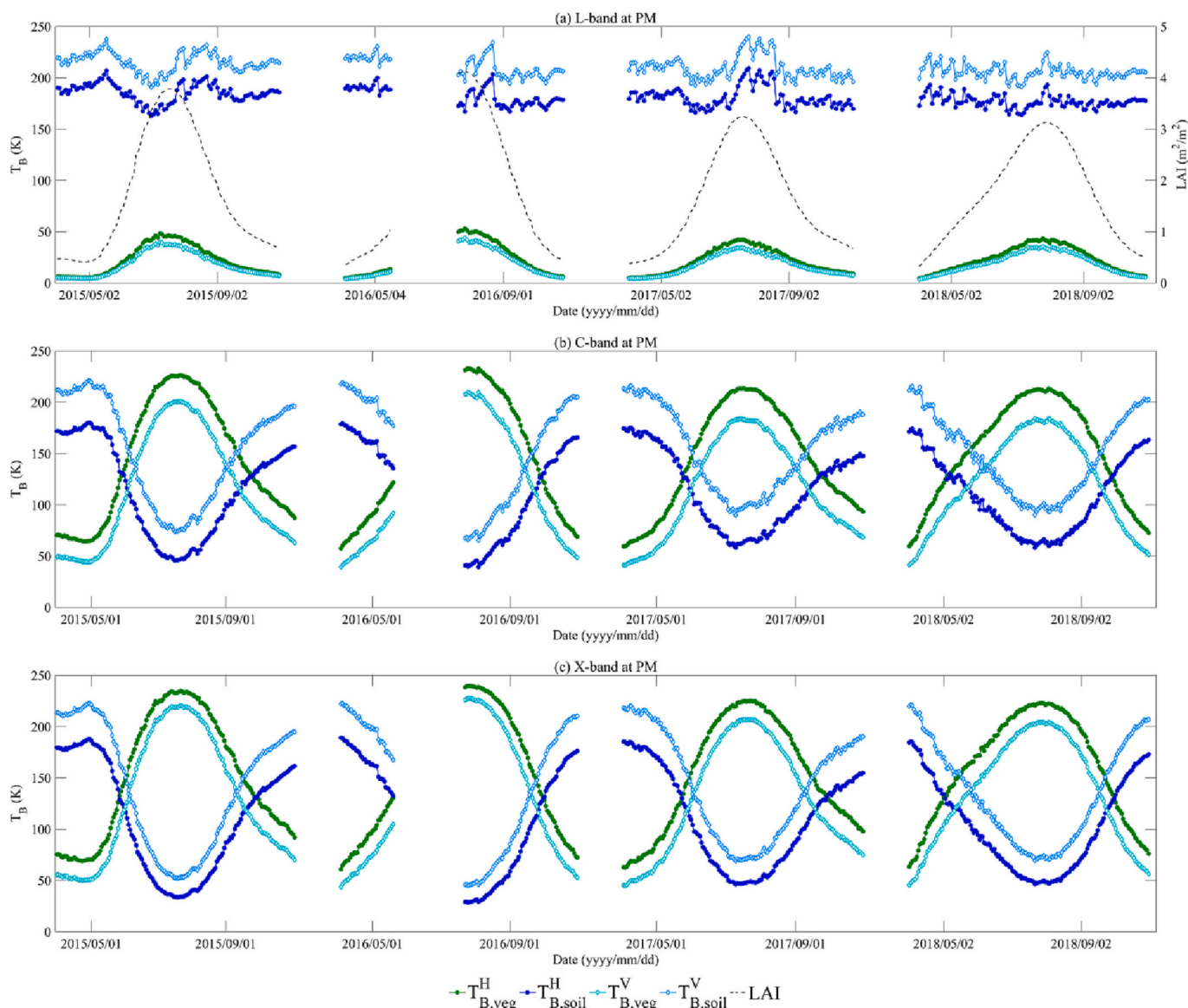
Fig. 4. Emission contributions produced by Sim2 for the three frequecies at PM: (a) L-, (b) C-, and (c) X-band.

growing season that is characterized by the MODIS LAI product in the TVG model (see Section 3.1). Similar result was also achieved by Moesinger et al. (2020) in grassland dominated regions.

4.3. Comparison of multi-frequency VOD products

As shown in Li et al. (2021), current satellite-based VOD products present comparable magnitudes at different frequencies, which is contrary to theory that the VOD exhibits frequency dependence as confirmed by Baur et al. (2019). To further explore this phenomenon, the magnitudes and seasonal patterns of current satellite-based VOD products are compared to the TVG derived VODs over the Tibetan grassland. Fig. 6a shows the time series of VOD derived either from the L-band SMAP and SMOS products (see Table 1) or from the TVG simulations during AM overpass due to the fact that the MT-DCA VOD product is only available at AM overpass. The SMAP VOD values (i.e. SMAP-SCA, SMAP-DCA, and MT-DCA) are much larger than the TVG VOD as also reported by Zheng et al. (2018b). The SMOS VOD values (i. e. SMOS-L3 and SMOS-IC) are closer to the TVG VOD but with larger variations that can be attributed to the impact of radio frequency interference (Dente et al., 2012b). It can be also found that the seasonal

dynamics of L-band VOD derived from current products are larger than the TVG VOD.

Fig. 6b and c show the VOD derived from the C- and X-band AMSR2 products (see Table 1) during PM overpass, respectively. The TVG VOD is also shown for comparison purpose. The seasonal changes of C-band VOD derived from the VODCA and LPRM products are smaller than the TVG VOD, whereby the corresponding values are much lower than the TVG VOD during the vegetation growth period from June to August. Similar to the C-band, the X-band VOD of the VODCA and LPRM are also much smaller than the TVG VOD during the vegetation growth period. On the contrary, the LPDR VOD is generally larger than the TVG VOD. Nevertheless, the seasonal dynamics of X-band VOD derived from current products are also smaller than the TVG VOD as the C-band.

In summary, both the TVG VOD and the satellite-based VOD products show similar seasonal pattern that generally follows the LAI variations, while different amplitudes can be noted between the TVG estimations and VOD retrievals. An interesting finding is worth pointing out that the amplitude of TVG VOD generally increases with increasing frequency especially from L- to C-band. However, this phenomenon is not obvious in current satellite-based VOD retrievals. Compared to the L-band and X-band products, the values of C-band VOD products show
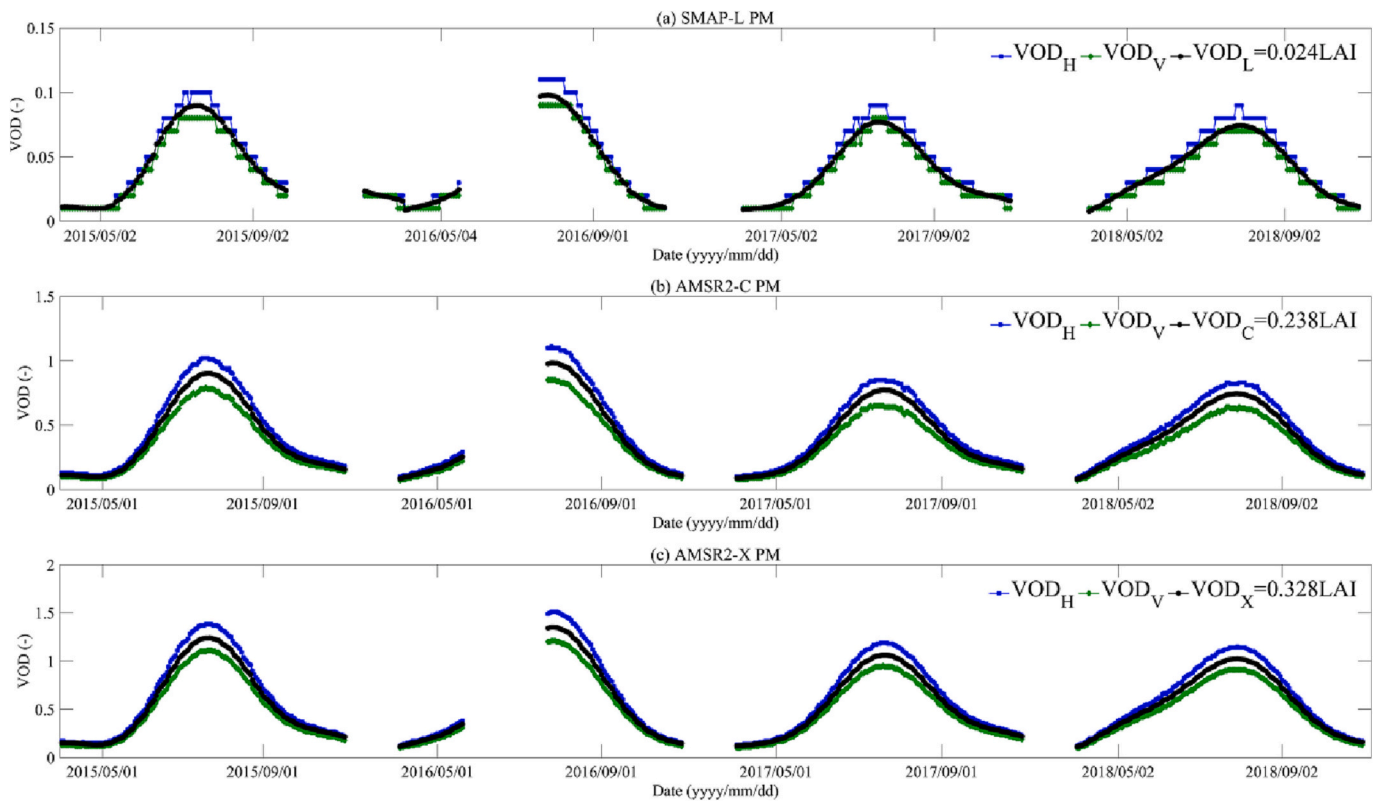
Fig. 5. Time series of VOD estimated based on the Sim2 simulations and their linear relationships with LAI for the three frequecies at PM: (a) L-, (b) C-, and (c) X-band.
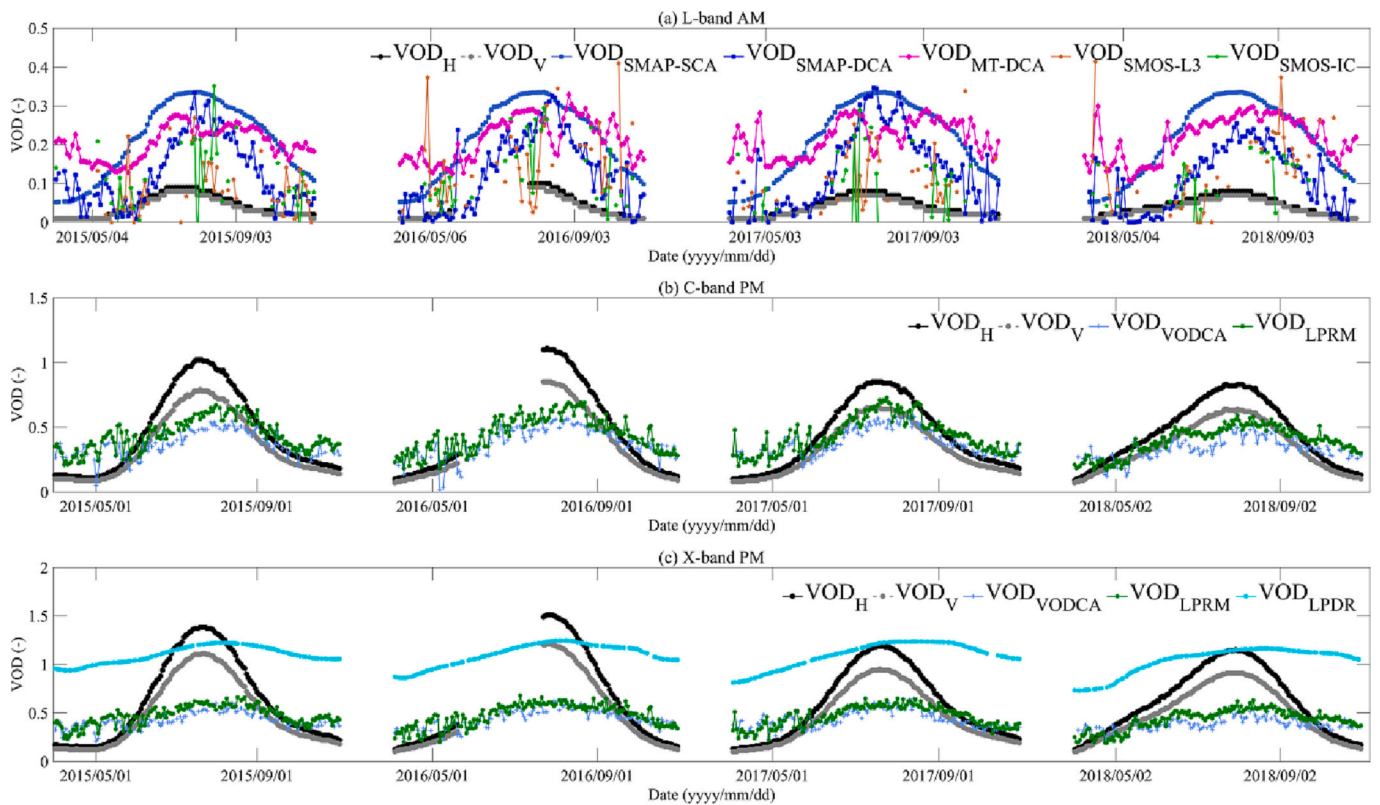

Fig. 6. Time series of VODs derived from current satellite products (SMAP and AMSR2) and TVG estimations for the three frequecies: (a) L-, (b) C-, and (c) X-band. The VOD_H and VOD_V stand for the TVG VOD computed for horizontal and vertical polarizations.

smaller differences in comparison to the TVG estimations. Large differences between the TVG derived VODs and VOD products generally occur at the summer peak, and the C-band products almost capture the peak of TVG estimations. Further discussion on the noted differences between the VOD products and TVG derived VODs is given in Section 5.

4.4. Sensitivity test of emission simulations

As shown in Sections 4.2 and 4.3, an identical physically-based model (i.e. the calibrated TVG model) with a single set of model parameter values shows the great potential to investigate the impact of frequency on simulating the land emission and associated components as well as estimating the VOD after isolating the impact of frequency on parameter values. A jump in behavior between L- and C-band and little difference between C- and X-band emission simulations and VOD estimations is found, which is attributed to the penetration capability of different frequencies, but the impact of observation angle cannot be isolated. Therefore, numerical experiments are performed in this section using the calibrated TVG model to further investigate the impact of microwave frequency and observation angle on the emission simulations and VOD estimations. The frequency under investigation includes P- (0.435 GHz), L- (1.41 GHz), S- (3.2 GHz), C- (6.925 GHz), X- (10.65 GHz), and K-band (18.7 GHz), which corresponds to the frequency configuration implemented by current operational satellites (e.g. SMAP, SMOS, and AMSR2) or planned missions (e.g. CIMR). The reason for the inclusion of P-, S-, and K-band is attributed to that it helps for investigating the jump behavior from low to high frequency in simulating emission and estimating VOD. The observation angles set for the simulations range from 0° to 60° with interval of 5°. The SM changes from 0.01 to 0.50 m³/m³ with interval of 0.01 m³/m³ and the LAI varies from 0.1 to 6.0 m²/m² with increment of 0.1 m²/m². The soil temperature is set to 20 °C, and values of other model parameters are identical to the Sim2 (see Tables 2 and 3). Three groups of soil and vegetation conditions are analyzed, i.e. low SM (0.10 m³/m³) and LAI (1.0 m²/m²), medium SM (0.30 m³/m³) and LAI (2.5 m²/m²), and high SM (0.50 m³/m³) and

LAI (5.0 m²/m²). The results for the second group are presented in Fig. 7 as examples, and those of first and third groups are shown in Figs. A1 and A2 (see Appendix A) due to similar results as the second group.

At different observation angles, values of both T_B^H and T_B^V simulations increase with increasing frequency from P- to C-band except the T_B^V simulation at large observation angles (e.g. 60° for the three groups). The increment increases with increasing angle for the T_B^H, while the T_B^V shows opposite trend that follow the Fresnel behavior. On the contrary, a slight decreasing trend can be noted for the T_B^H simulations when frequency is further increased from C- to K-band due to the decrease of soil contribution. The values of soil emission are comparable to each other for P-, L-, and S-band especially at low observation angle ($\leq 40°$), and decrease with increasing frequency from S- to K-band. Notably, the decline is significant from S- to C-band. In contrast, the values of vegetation contribution generally increase with increasing frequency especially from S- to C-band, and also increase with increasing vegetation coverage (i.e. LAI values) particularly for frequency between S- and K-band. Accordingly, the estimated VOD values increase with increasing vegetation coverage and frequency especially from S- to K-band as well. In addition, the polarization-dependence of VOD becomes more apparent with the increasing observation angle and frequency. This means the polarization-independence assumption of VOD will be invalid at relatively large observation angle especially at high frequency. Nevertheless, the polarization-independence assumption implemented by current retrieval algorithms of SMAP mission (L-band, 40°) (O'Neill et al., 2020) sounds reasonable. The soil contribution generally dominates the total emission at low frequencies especially at P- and L-band, which confirms the superiority of using P- and L-band to detect SM dynamics. The contribution of soil emission generally decreases with increasing vegetation coverage and frequency due to increasing vegetation attenuation.

For different frequencies, the differences between the soil emission at horizontal and vertical polarizations increase with increasing observation angle especially at low frequency (e.g. P-, L- and S-band) that follow the Fresnel behavior, which leads to similar trends noted for the
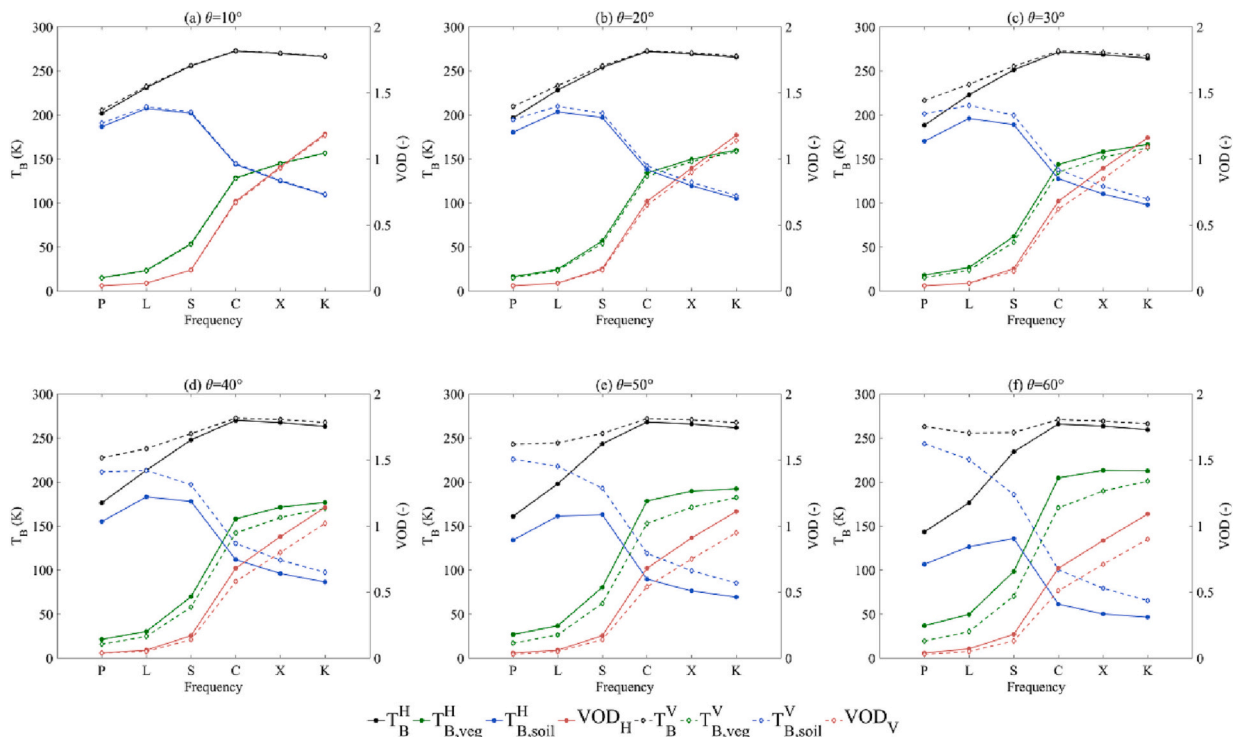

Fig. 7. Effect of frequency and observation angle on emission simulation with SM and LAI set as 0.30 m³/m³ and 2.5 m²/m². (a) $\theta = 10°$, (b) $\theta = 20°$, (c) $\theta = 30°$, (d) $\theta = 40°$, (e) $\theta = 50°$, and (f) $\theta = 60°$.

differences between T_B^H and T_B^V. Similarly, the differences between the vegetation emission and VOD at horizontal and vertical polarizations also increase with increasing observation angle especially at high frequency (e.g. C-, X-, K-band). In general, both T_B and soil emission monotonically decrease with increase of SM due to decrease of soil emissivity at low frequency (e.g. P-, L-, S-band), and the changes are much smaller at high frequency and vegetation coverage due to increasing vegetation attenuation.

5. Discussion

Microwave observations at multiple frequencies as implemented by the CIMR mission have received increasing research interests due to its capability to provide multi-channel information of soil and vegetation with multi-frequency configuration. Recently, Zhao et al. (2021) have shown that increasing the number of observation channels (e.g. frequency and/or observation angle) could increase the degree of information and make the SM retrieval more robust. Although several parametric (e.g. CMEM) and theoretical models (e.g. TVG model) have been developed to allow for simultaneously simulating the microwave observations at multiple frequencies, up to now no work was carried out to validate their performance in capturing the satellite observations at different frequencies. In addition, the theorical model was usually calibrated using satellite observations at each individual frequency to obtain the unmeasurable physical features of vegetation and soil parameters at the satellite footprint. This often leads to different parameter values for different frequencies at the same site (e,g. Dente et al., 2014; Wang et al., 2018; Bai et al., 2019), which is against the fact that these parameters in the theoretical models are only dependent on site condition instead of frequency. In other words, these parameters may lose their physical interpretability and become "effective parameters" by imposing different values for different frequencies. As the first attempt, this paper shows the validity of using an identical physically-based model (i.e. TVG model) with a single set of model parameter values to reproduce well the SMAP L-band and AMSR2 C- and X-band T_B observations over Tibetan grasslands. As such, the dependence of emission components and VOD on frequency can be elaborated (see Sections 4.2–4.4) after isolating the frequency dependence of parameter values.

As shown in Sections 4.2 and 4.3, the TVG derived VODs show frequency dependence with values and associated amplitudes increasing with frequency. The values at C- and X-band are more than ten times larger than the one of L-band. This is in line with the theory that the VOD senses the vegetation canopy with different layer and depths due to different penetration capability of observation frequency (Baur et al., 2019; Moesinger et al., 2020). On the contrary, the satellite-based VOD retrievals have almost the same magnitude at the L-, C-, and X-band as also reported by Li et al. (2021). One possible reason for this can be related to the compensation between surface roughness and vegetation effects when retrieving both VOD and SM from satellites. This indicates that the satellite VOD may be only an effective vegetation index tuning for SM retrieval rather than a physical parameter that represents the intensity of microwave extinction effects within the vegetation canopy (Wigneron et al., 2017). In other words, the satellite VOD may have different meanings in comparison to the TVG estimations with physical significance, which nevertheless, can be used to monitor the vegetation dynamics (Fan et al., 2019; Wigneron et al., 2020).

Recently, Zhao et al. (2021) indicated that frequency-dependence of VOD should be considered in the Tau-Omega model (Mo et al., 1982) to improve the SM retrievals based on a multi-frequency approach. In addition, our study also shows that the dependence of VOD on observation angle and polarization should not be ignored as well (e.g. see Fig. 7). Based on the results of sensitivity test using the calibrated TVG model (see Section 4.4), a new parameterization has thus been further developed in this study to characterize the dependence of VOD on the frequency, observation angle, and polarization for grassland (see Appendix B). Specifically, Eq. (B4) is proposed to represent the impact of

frequency, observation angle, and polarization on the relationships found between the VOD and LAI. As in Wigneron et al. (1995, 2007), the coefficient tt_{p_vod} is introduced to represent the impact of polarization and observation angle on the VOD, and the values of which are found to be different at the horizontal and vertical polarizations (see Table B1). Fig. 8 shows the scatterplots between the TVG derived VOD based on the results of sensitivity test and those estimated by using the new parameterization (i.e. Eq. (B4)). The corresponding RMSE and ubRMSE computed between them are also shown. The scatterplots and statistical indicators generally show that the new parameterizations are able to reproduce well the TVG derived VOD at different frequencies, leading to RMSEs and ubRMSEs of less than 0.072 and 0.068, respectively. The new parameterization could thus provide a way to address the dependence of VOD on the frequency, observation angle, and polarization in the land emission simulation at multiple frequencies.

As shown in Zhao et al. (2021), the probability that the land emission simulations will not match the observations may increase by increasing the number of observation frequencies while the VOD and surface roughness parameterizations are not appropriate, which could further limit the retrieval performance. The VOD parameterization developed in this study may help to address this issue, leading to better retrieval of VOD for different frequencies with physical interpretability. For instance, the newly developed VOD parameterization can be incorporated into the framework of CMEM and then be combined with the multi-channel collaborative algorithm developed by Zhao et al. (2021) to retrieve the SM and VOD based on SMAP and AMSR2 observations at different frequencies. As such, the performance of the new VOD parameterization on retrieving the SM and providing constraint to the VOD retrievals for different frequencies can be validated. Since the SM and VOD retrievals are also often affected by the parameterization of surface roughness and adopted retrieval algorithm (Wigneron et al., 2017; Gao et al., 2021), additional work is still needed to test above guess. Nevertheless, Zheng et al. (2018b) have shown the potential of improving land emission simulation and SM retrieval at L-band by incorporating the TVG derived VOD parameterization. In addition, Baur et al. (2019) have demonstrated the benefit of estimating relative canopy absorption and scattering at L-, C- and X-bands through minimizing differences between multi-frequency observations and Tau-Omega model simulations. It was shown that the estimated VOD at C- and X-band have sensitivity to leaf phenology while that of L-band is sensitive to changes in water content of stems and woody parts of vegetation. This indicates that VOD estimations/retrievals across microwave frequencies could provide new insights into studying plant water storage and hydraulic strategies.

In summary, microwave observations at multiple frequencies can provide complementary information for better understanding the interaction between the observed signal and land surface, and separating specific emission mechanisms associated with different land conditions as well as estimating their properties. An identical physically-based model (i.e. TVG model) with a single set of model parameter values constrained by the multi-frequency observations can be used to validate the frequency-dependence of VOD and develop appropriate parameterization by isolating the impact of frequency on parameter values. The newly developed VOD parameterization could further provide constraint for retrieving VOD at different frequencies with physical interpretability based on multi-frequency observations. Better estimation or retrieval of VOD across different frequencies may lead to better understanding of plant physiological characteristic (i.e. water storage and hydraulic strategies).

6. Conclusions

In this paper, the potential of using a discrete scattering model with a single set of model parameter values to simulate land surface emission and estimate vegetation properties at multiple frequencies is investigated. Specifically, the validity of TVG model in simultaneously
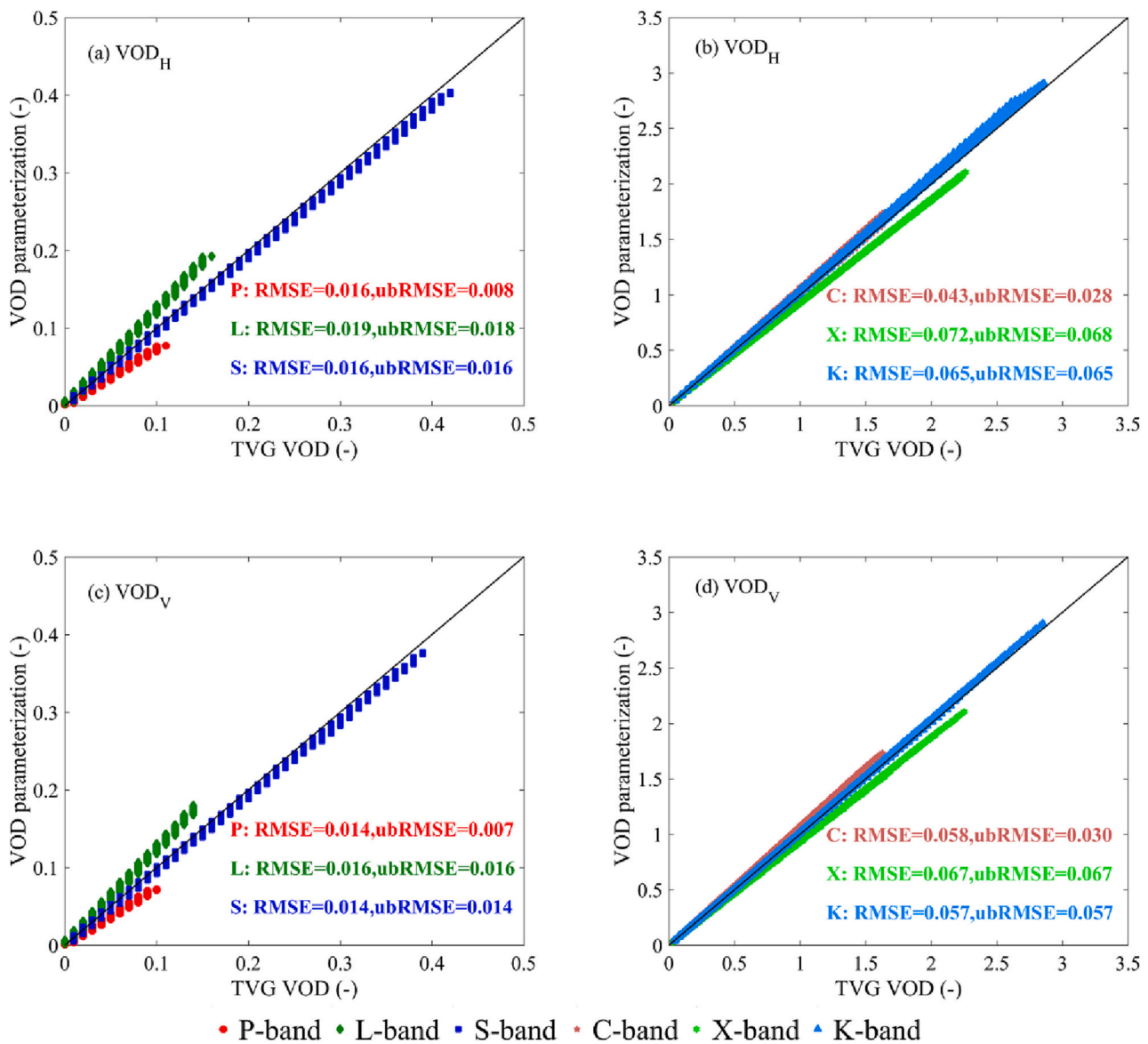
Fig. 8. Scatterplot between VOD obtained from TVG simulation and Eq. (B4) for (a, c) P-, L-, S-band and (b, d) C-, X-, K-band at horizontal (a, b) and (c, d) vertical polarizations.

reproducing the SMAP L-band and AMSR2 C- and X-band T_B^p observations over the Tibetan grassland ecosystem is evaluated. Two model calibration strategies, i.e. frequency-specific calibration and multi-frequency calibration, are implemented to find the suitable set of model parameter values. The calibrated TVG model is further used to estimate the VOD at different frequencies, as well as to investigate the impact of microwave frequency and observation angle on the emission simulations. Besides, the differences between the TVG derived VOD and current satellite retrievals are examined in detail, and new parameterization is developed for VOD at multi-frequency.

Fairly good agreements are achieved between the calibrated TVG simulations and multi-frequency satellite observations for both calibration and validation periods. Comparison between the time series of TVG simulations and satellite observations shows that the calibrated TVG model captures well the seasonal dynamics and magnitudes of both SMAP and AMSR2 T_B^p observations especially at L- and C-band. The performance of multi-frequency calibration is comparable to the frequency-specific calibration, confirming the validity of simulating multi-frequency T_B^p observations using an identical physically-based model (i.e. TVG model) with a single set of model parameters. As

such, the dependence of VOD on frequency can be elaborated after isolating the impact of frequency on parameter values. The VOD values estimated based on the TVG simulations generally follow the dynamics of vegetation growth and can be linearly correlated to the LAI variations for the three frequencies. Both values and seasonal amplitudes of TVG derived VOD increase with increasing frequency, while current satellite-based retrievals have almost the same magnitude at the L-, C-, and X-band. The explanation for this can be that the satellite-based retrievals may have different meanings in comparison to the TVG estimations in terms of physical significance. On the one hand, the TVG derived VOD is in line with the theoretical principle that the vegetation emission contribution and extinction effect increase with increasing frequency, leading to larger VOD values at higher frequency. On the other hand, the satellite VOD is more like a vegetation index that compensate between surface roughness and vegetation effects during the SM and VOD retrievals. In addition, results of sensitivity test based on the calibrated TVG model show that polarization-dependence of VOD becomes more apparent with increasing observation angle and frequency. Based on the results of sensitivity tests, new parameterization has been further developed to characterize the dependence of VOD on the frequency,

observation angle, and polarization for grassland.

This study demonstrates the validity of using an identical physically-based model (i.e. TVG model) with a single set of model parameter values to simultaneously reproduce SMAP and AMSR2 observations and estimate multi-frequency vegetation properties by isolating the impact of frequency on parameter values. Frequency-dependence of VOD is confirmed by the TVG estimations, and these results are further used to develop a new VOD parameterization that can be incorporated into current parametric model such as the CMEM to better retrieve the SM and VOD of different frequencies with physical interpretability based on multi-frequency observations as planned by the CIMR mission. Better estimation or retrieval of VOD across different frequencies could provide new sights for quantifying vegetation water storage and hydraulic strategies. In addition, the calibrated TVG model could be used as a testbed for validating the future satellite missions (e.g. CIMR and Terrestrial Water Resources Satellite) due to its good performance (Dente et al., 2014; Zheng et al., 2021b) after isolating the impact of frequency or sensor on parameter values. However, it should be noted that the results obtained are based on the assumption that the surface SM is vertically uniform within the emission depth of different frequencies as in Baur et al. (2019). Additional work is still needed to quantify the impact of this assumption via coupling the calibrated TVG model with a land surface model that enables simulating the vertical SM gradient in the surface layer as in Zheng et al. (2017b).

CRediT authorship contribution statement

Xiaojing Bai: Conceptualization, Methodology, Formal analysis, Writing – original draft, Writing – review & editing. **Donghai Zheng:** Conceptualization, Methodology, Data curation, Writing – review & editing, Supervision, Funding acquisition. **Xin Li:** Writing – review & editing. **Jean-Pierre Wigneron:** Writing – review & editing. **Rogier van der Velde:** Writing – review & editing. **Pei Zhang:** Writing – review & editing. **Zhongbo Su:** Writing – review & editing.

Declaration of Competing Interest

The authors declare that they have no known competing financial interests or personal relationships that could have appeared to influence the work reported in this paper.

Data availability

Data will be made available on request.

Acknowledgements

Appendix A. Sensitivity test of emission simulations

Fig. A1. Effect of frequency and observation angle on emission simulation with SM and LAI set as 0.10 m³/m³ and 1.0 m²/m². (a) $\theta = 10°$, (b) $\theta = 20°$, (c) $\theta = 30°$, (d) $\theta = 40°$, (e) $\theta = 50°$, and (f) $\theta = 60°$.
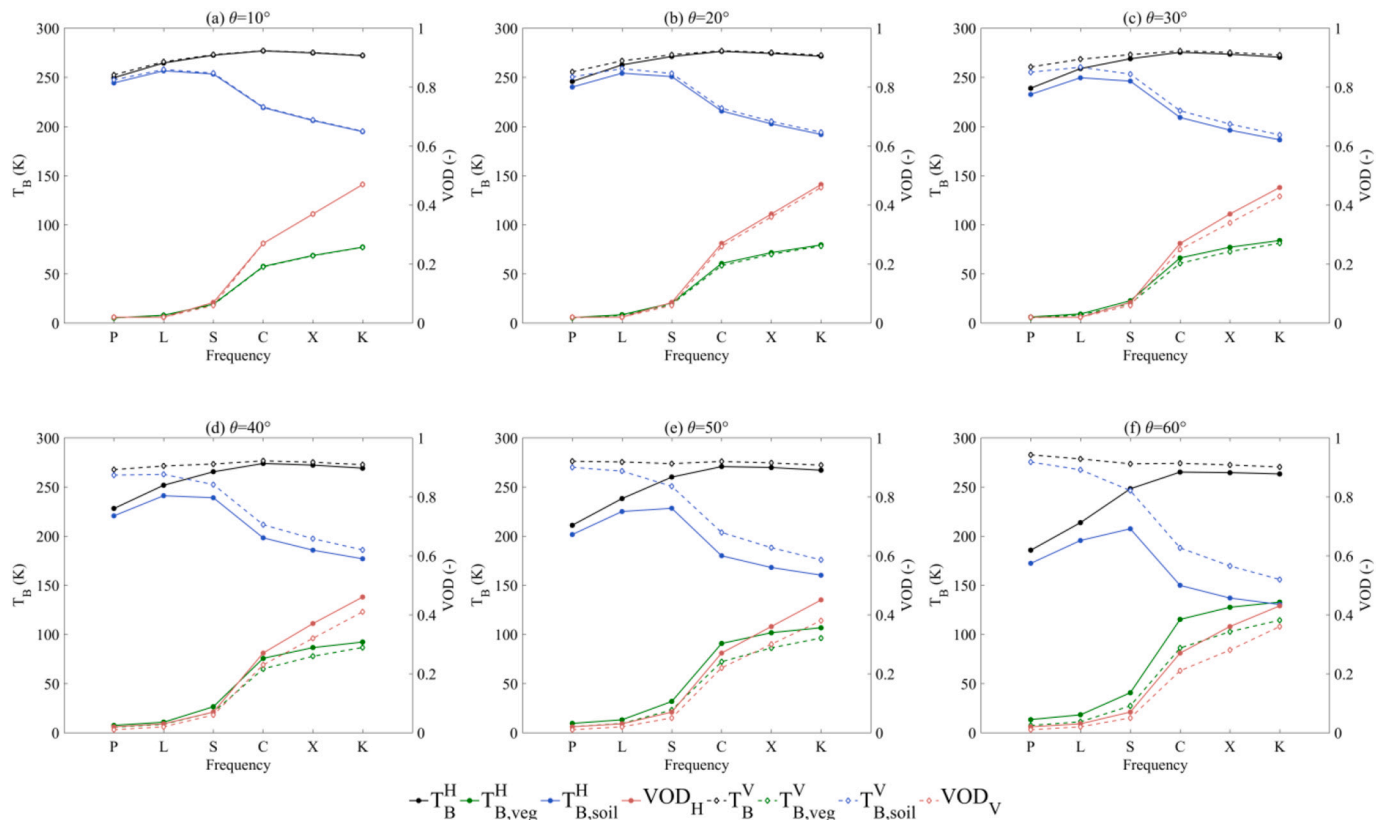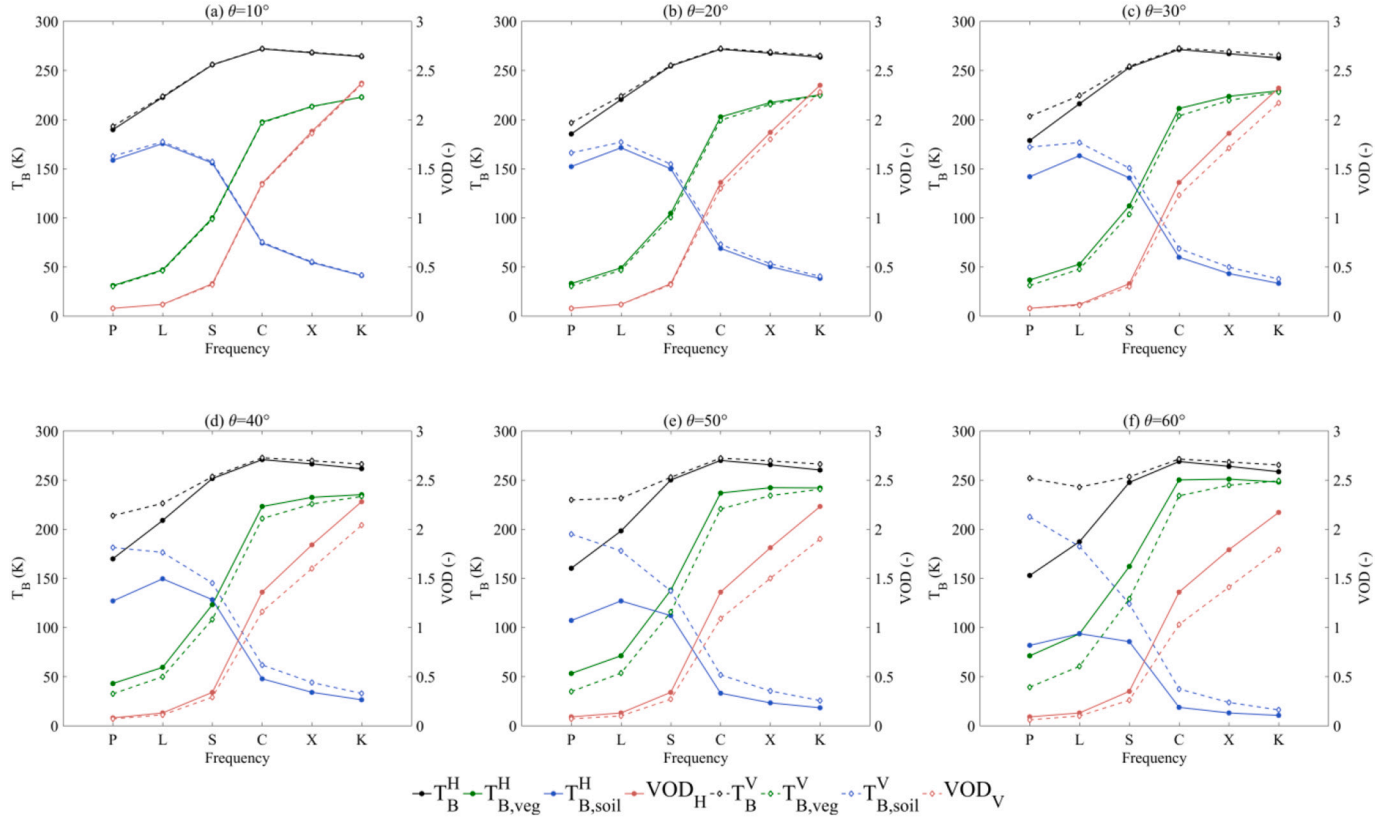
Fig. A2. Effect of frequency and observation angle on emission simulation with SM and LAI set as 0.50 m^3/m^3 and 5.0 m^2/m^2. (a) $\theta = 10°$, (b) $\theta = 20°$, (c) $\theta = 30°$, (d) $\theta = 40°$, (e) $\theta = 50°$, and (f) $\theta = 60°$.

Appendix B. New parameterization of VOD

As implemented by the SMOS mission (Wigneron et al., 2017), the dependence of VOD on observation angle and polarization can be expressed as,

$$VOD^p = VOD_{NAD} \times \left(sin^2\theta \times tt_{p\_vod} + cos^2\theta \right) \tag{B1}$$

$$VOD_{NAD} = b' \times LAI + b'' \tag{B2}$$

where the VOD$_{NAD}$ is the value of VOD at nadir (i.e. $\theta = 0°$), and the parameter tt_{p_vod} allows for the dependence of VOD on observation angle and polarization to be accounted for. The parameters b' and b'' are originally assumed to be mainly dependent on the vegetation type (Wigneron et al., 2017), which is adopted in this study to characterize the dependence of VOD on frequency as well.

Based on the results of sensitivity test using the calibrated TVG model (see Section 4.4), the scatterplot between the VOD$_{NAD}$ and LAI at different frequencies are shown in (a) and (b) of Fig. B1. From the plot, it is found that the VOD$_{NAD}$ and LAI shows a linear relationship at different frequencies, whereby the value of b'' can be set to zero, and the value of b' shows frequency-dependent. A linear function is thus further adopted to account for the dependence of b' on the frequency as,

$$b' = bb' \times k + bb'' \tag{B3}$$

where bb' and bb'' are fitting coefficients, and k is the wavenumber ($k = 2\pi/\lambda$, λ is the wavelength). Combine above three equations, the dependence of VOD on frequency, polarization and observation angle can be written as,

$$VOD^p = \left[\left(bb' \times k + bb'' \right) \times LAI \right] \times \left(sin^2\theta \times tt_{p\_vod} + cos^2\theta \right) \tag{B4}$$

In this study, the coefficients in Eq. B4 are derived using the results of TVG sensitivity test (see Section 4.4) for grassland, and relevant results are given in Table B1. Since a sharp increase is observed for the VOD when the frequency increases from the S- to C-band (see Fig. 7), the coefficients in Eq. (B4) is fitted for two frequency ranges, i.e. P-, L-, S-band and C-, X-, K-band. For example, with L-band (1.41 GHz) and incidence angle of 40°, it is written as $VOD^H = 0.031 \times LAI$ and $VOD^V = 0.027 \times LAI$. The values (0.031 and 0.027) are very close to 0.024 in Eq. 4.
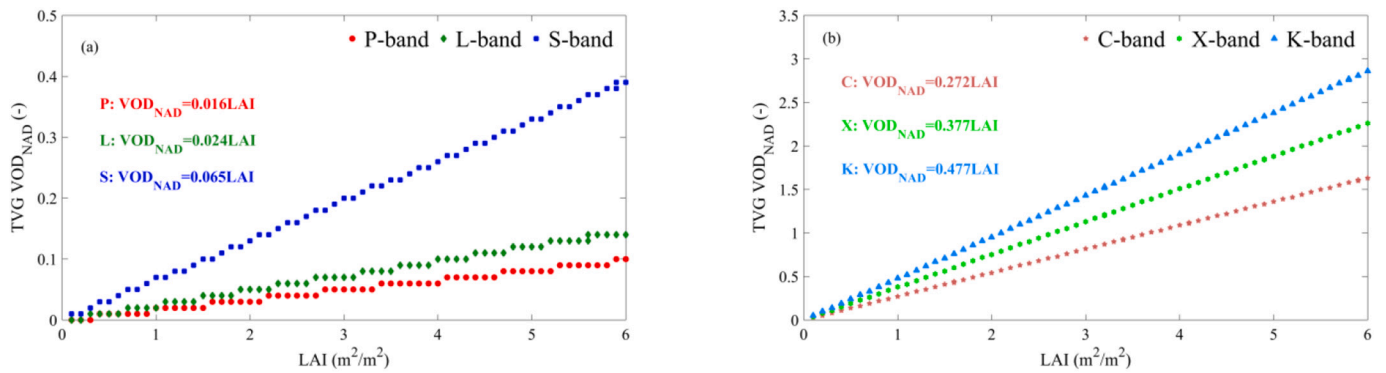
Fig. B1. Scatter between VOD_{NAD} and LAI at P-, L-, S-band (a) and at C-, X-, K-band (b).

Table B1

List of fitting coefficient used in Eq. (B4).

Frequency	Polarization	bb'	bb''	tt_{p_vod}
P-, L-, S-band	H	0.088	0.004	1.093
	V			0.716
C-, X-, K-band	H	0.079	0.175	0.923
	V			0.657

References

Al Bitar, A., Mialon, A., Kerr, Y.H., Cabot, F., Richaume, P., Jacquette, E., Quesney, A., Mahmoodi, A., Tarot, S., Parrens, M., Al-Yaari, A., Pellarin, T., Rodriguez-Fernandez, N., Wigneron, J.P., 2017. The global SMOS level 3 daily soil moisture and brightness temperature maps. Earth Syst. Sci. Data 9, 293–315.

Bai, X., Zeng, J., Chen, K.S., Li, Z., Zeng, Y., Wen, J., Wang, X., Dong, X., Su, Z., 2019. Parameter optimization of a discrete scattering model by integration of global sensitivity analysis using SMAP active and passive observations. IEEE Trans. Geosci. Remote Sens. 57 (2), 1084–1099.

Baur, M.J., Jagdhuber, T., Feldman, A.F., Akbar, R., Entekhabi, D., 2019. Estimation of relative canopy absorption and scattering at L-, C- and X-bands. Remote Sens. Environ. 233, 111384.

Birchak, J.R., Gardner, C.G., Hipp, J.E., Victor, J.M., 1974. High dielectric constant microwave probes for sensing soil moisture. Proc. IEEE 62, 93–98.

Bracaglia, M., Ferrazzoli, P., Guerriero, L., 1995. A fully polarimetric multiple scattering model for crops. Remote Sens. Environ. 54, 170–179.

Chan, S.K., Bindlish, R., O'Neill, P.E., Njoku, E., Jackson, T., Colliander, A., Chen, F., Burgin, M., Dunbar, S., Piepmeier, J., Yueh, S., Entekhabi, D., Cosh, M.H., Caldwell, T., Walker, J., Wu, X., Berg, A., Rowlandson, T., Pacheco, A., McNairn, H., Thibeault, M., Martinez-Fernandez, J., Gonzalez-Zamora, A., Seyfried, M., Bosch, D., Starks, P., Goodrich, D., Prueger, J., Palecki, M., Small, E.E., Zreda, M., Calvet, J.C., Crow, W.T., Kerr, Y., 2016. Assessment of the SMAP passive soil moisture product. IEEE Trans. Geosci. Remote Sens. 54 (8), 4994–5007.

Chauhan, N.S., Le Vine, D.M., Lang, R.H., 1994. Discrete scatter model for microwave radar and radiometer response to corn: comparison of theory and data. IEEE Trans. Geosci. Remote Sens. 32 (2), 416–426.

Choudhury, B.J., Schmugge, T.J., Mo, T., 1982. A parameterization of effective soil temperature for microwave emission. J. Geophys. Res. 87 (C2), 1301–1304.

Colliander, A., Jackson, T.J., Bindlish, R., Chan, S., Das, N., Kim, S.B., Cosh, M.H., Dunbar, R.S., Dang, L., Pashaian, L., Asanuma, J., Aida, K., Berg, A., Rowlandson, T., Bosch, D., Caldwell, T., Caylor, K., Goodrich, D., al Jassar, H., Lopez-Baeza, E., Martínez-Fernández, J., González-Zamora, A., Livingston, S., McNairn, H., Pacheco, A., Moghaddam, M., Montzka, C., Notarnicola, C., Niedrist, G., Pellarin, T., Prueger, J., Pulliainen, J., Rautiainen, K., Ramos, J., Seyfried, M., Starks, P., Su, Z., Zeng, Y., van der Velde, R., Thibeault, M., Dorigo, W., Vreugdenhil, M., Walker, J.P., Wu, X., Monerris, A., O'Neill, P.E., Entekhabi, D., Njoku, E.G., Yueh, S., 2017. Validation of SMAP surface soil moisture products with core validation sites. Remote Sens. Environ. 191, 215–231.

de Nijs, A.H.A., Parinussa, R.M., de Jeu, R.A.M., Schellekens, J., Holmes, T.R.H., 2015. A methodology to determine radio-frequency interference in AMSR2 observations. IEEE Trans. Geosci. Remote Sens. 53 (9), 5148–5159.

de Rosnay, P., Drusch, M., Boone, A., Balsamo, G., Decharme, B., Harris, P., Kerr, Y., Pellarin, T., Polcher, J., Wigneron, J.P., 2009. AMMA land surface model intercomparison experiment coupled to the community microwave emission model: ALMIP-MEM. J. Geophys. Res. 114, D05108.

de Rosnay, P., Muñoz-Sabater, J., Albergel, C., Isaksen, L., English, S., Drusch, M., Wigneron, J.P., 2020. SMOS brightness temperature forward modelling and long term monitoring at ECMWF. Remote Sens. Environ. 237, 111424.

Della Vecchia, A., Ferrazzoli, P., Guerriero, L., Rahmoune, R., Paloscia, S., Pettinato, S., Santi, E., 2010. Modeling the multifrequency emission of broadleaf forests and their components. IEEE Trans. Geosci. Remote Sens. 48, 260–272.

Dente, L., Ferrazzoli, P., Su, Z., van der Velde, R., Guerriero, L., 2014. Combined use of active and passive microwave satellite data to constrain a discrete scattering model. Remote Sens. Environ. 155, 222–238.

Dente, L., Vekerdy, Z., Wen, J., Su, Z., 2012a. Maqu network for validation of satellite-derived soil moisture products. Int. J. Appl. Earth Obs. Geoinf. 17, 55–65.

Dente, L., Su, Z., Wen, J., 2012b. Validation of SMOS soil moisture products over the Maqu and Twente regions. Sensors 12, 9965–9986.

Donlon, C.J., 2018. Copernicus Imaging Microwave Radiometer (CIMR) mission requirements document. version 1.5 (Tech. Rep.). European Space Agency, Noordwijk, Netherlands.

Drusch, M., Wood, E., Jackson, T., 2001. Vegetative and atmospheric corrections for soil moisture retrieval from passive microwave remote sensing data: results from the southern Great Plains hydrology experiment 1997. J. Hydromet. 2, 181–192.

Du, J., Kimball, J.S., Jones, L.A., Kim, Y., Glassy, J., Watts, J.D., 2017. A global satellite environmental data record derived from AMSR-E and AMSR2 microwave earth observations. Earth Syst. Sci. Data 9, 791–808.

Entekhabi, D., Njoku, E.G., O'Neill, P.E., Kellogg, K.H., Crow, W.T., Edelstein, W.N., Entin, J.K., Goodman, S.D., Jackson, T.J., Johnson, J., Kimball, J., Piepmeier, J.R., Koster, R.D., Martin, N., McDonald, K.C., Moghaddam, M., Moran, S., Reichle, R., Shi, J.C., Spencer, M.W., Thurman, S.W., Tsang, L., Van Zyl, J., 2010. The soil moisture active passive (SMAP) mission. Proc. IEEE 98, 704–716.

Eom, H.J., Fung, A.K., 1984. A scatter model for vegetation up to Ku-band. Remote Sens. Environ. 15, 185–200.

Fan, L., Wigneron, J.-P., Ciais, P., Chave, J., Brandt, M., Fensholt, R., Saatchi, S.S., Bastos, A., Al-Yaari, A., Hufkens, K., Qin, Y., Xiao, X., Chen, C., Myneni, R., Fernandez-Moran, R., Mialon, A., Rodriguez-Fernandez, N.J., Kerr, Y., Tian, F., Peñuelas, J., 2019. Satellite-observed pantropical carbon dynamics. Nat. Plants 5 (9).

Fernandez-Moran, R., Al-Yaari, A., Mialon, A., Mahmoodi, A., Al Bitar, A., De Lannoy, G., Rodriguez-Fernandez, N., Lopez-Baeza, E., Kerr, Y., Wigneron, J.P., 2017. SMOS-IC: an alternative SMOS soil moisture and vegetation optical depth product. Remote Sens. 9, 457.

Ferrazzoli, P., Guerriero, L., 1996. Passive microwave remote sensing of forests: a model investigation. IEEE Trans. Geosci. Remote Sens. 34 (2), 433–440.

Ferrazzoli, P., Guerriero, L., Wigneron, J.P., 2002. Simulating L-band emission of forests in view of future satellite applications. IEEE Trans. Geosci. Remote Sens. 40 (12), 2700–2708.

Fung, A.K., 1994. Microwave Scattering and Emission Models and Their Applications. Artech House, Norwell, MA, USA.

Gao, L., Ebtehaj, A., Chaubell, M.J., Sadeghi, M., Li, X., Wigneron, J.-P., 2021. Reappraisal of SMAP inversion algorithms for soil moisture and vegetation optical depth. In: Remote Sens, Environ., p. 264

Guerriero, L., Ferrazzoli, P., Vittucci, C., Rahmoune, R., Aurizzi, M., Mattioni, A., 2016. L-band passive and active signatures of vegetated soil: simulations with a unified model. IEEE J.Sel. Top. Appl. Earth Obs. Remote Sens. 9, 2520–2531.

Holmes, T.R.H., Drusch, M., Wigneron, J.P., de Jeu, R.A.M., 2008. A global simulation of microwave emission: error structures based on output from ECMWF's operational integrated forecast system. IEEE Trans. Geosci. Remote Sens. 46 (3), 846–856.

Imaoka, K., Kachi, M., Fujii, H., Murakami, H., Hori, M., Ono, A., Igarashi, T., Nakagawa, K., Oki, T., Honda, Y., Shimoda, H., 2010. Global change observation mission (GCOM) for monitoring carbon, water cycles, and climate change. Proc. IEEE 98, 717–734.

Jackson, T., O'Neill, P., 1990. Attenuation of soil microwave emission by corn and soybeans at 1.4 and 5 GHz. IEEE Trans. Geosci. Remote Sens. 28 (5), 978–980.

Jackson, T.J., Schmugge, T.J., 1991. Vegetation effects on the Microwave emission of soils. Remote Sens. Environ. 36, 203–212.

Karam, M.A., 1997. A physical model for microwave radiometry of vegetation. IEEE Trans. Geosci. Remote Sens. 35 (4), 1045–1058.

Karthikeyan, L., Pan, M., Konings, A.G., Piles, M., Fernandez-Moran, R., Nagesh Kumar, D., Wood, E.F., 2019. Simultaneous retrieval of global scale vegetation optical depth, surface roughness, and soil moisture using X-band AMSR-E observations. Remote Sens. Environ. 234, 111473.

Kerr, Y.H., Waldteufel, P., Wigneron, J.P., Martinuzzi, J.M., Font, J., Berger, M., 2001. Soil moisture retrieval from space: the soil moisture and ocean salinity (SMOS) mission. IEEE Trans. Geosci. Remote Sens. 39 (8), 1729–1735.

Kirdyashev, K., Chukhlantsev, A., Shutko, A., 1979. Microwave radiation of the earth's surface in the presence of vegetation cover. Radiotekhnika i Elektronika 24, 256–264.

Konings, A.G., Piles, M., Das, N., Entekhabi, D., 2017. L-band vegetation optical depth and effective scattering albedo estimation from SMAP. Remote Sens. Environ. 198, 460–470.

Konings, A.G., Piles, M., Rotzer, K., McColl, K., Chan, S.K., Entekhabi, D., 2016. Vegetation optical depth and scattering albedo retrieval using time series of dual-polarized L-band radiometer observations. Remote Sens. Environ. 172, 178–189.

Kornelsen, K.C., Coulibaly, P., 2013. Advances in soil moisture retrieval from synthetic aperture radar and hydrological applications. J. Hydrol. 476, 460–489.

Kurum, M., Lang, R.H., O'Neill, P.E., Joseph, A.T., Jackson, T.J., Cosh, M.H., 2011. A first-order radiative transfer model for microwave radiometry of forest canopies at L-band. IEEE Trans. Geosci. Remote Sens. 49 (9), 3167–3179.

Lang, R.H., 1981. Electromagnetic backscattering from a sparse distribution of lossy dielectric scatterers. Radio Sci. 16, 15–30.

Lemmetyinen, J., Schwank, M., Rautiainen, K., Kontu, A., Parkkinen, T., Mätzler, C., Wiesmann, A., Wegmüller, U., Derksen, C., Toose, P., Roy, A., Pulliainen, J., 2016. Snow density and ground permittivity retrieved from L-band radiometry: application to experimental data. Remote Sens. Environ. 180, 377–391.

LeVine, D.M., Meneghini, R., Lang, R.H., Seker, S.S., 1983. Scattering from arbitrarily oriented dielectric disks in the physical optics regime. J. Opt. Soc. Am. 73, 1255–1262.

Li, X., Wigneron, J.-P., Fan, L., Frappart, F., Yueh, S.H., Colliander, A., Ebtehaj, A., Gao, L., Fernandez-Moran, R., Liu, X., Wang, M., Ma, H., Moisy, C., Ciais, P., 2022. A new SMAP soil moisture and vegetation optical depth product (SMAP-IB): algorithm, assessment and inter-comparison. Remote Sens. Environ. 271, 112921.

Li, X., Wigneron, J.P., Frappart, F., Fan, L., Ciais, P., Fensholt, R., Entekhabi, D., Brandt, M., Kongings, A.G., Liu, X., Wang, M., Al-Yaari, A., Moisy, C., 2021. Global-scale assessment and inter-comparison of recently developed/reprocessed microwave satellite vegetation optical depth products. Remote Sens. Environ. 253, 112208.

Li, X., Al-Yaari, A., Schwank, M., Fan, L., Frappart, F., Swenson, J., Wigneron, J.P., 2020. Compared performances of SMOS-IC soil moisture and vegetation optical depth retrievals based on tau-omega and two-stream microwave emission models. Remote Sens. Environ. 236, 111502.

Liu, Y.Y., de Jeu, R.A.M., McCabe, M.F., Evans, J.P., van Dijk, A.I.J.M., 2011. Global long-term passive microwave satellite-based retrievals of vegetation optical depth. Geophys. Res. Lett. 38, L18402.

Mätzler, C., 1994. Microwave (1–100 GHz) dielectric model of leaves. IEEE Trans. Geosci. Remote Sens. 32 (5), 947–949.

Mecklenburg, S., Drusch, M., Kaleschke, L., Rodriguez-Fernandez, N., Reul, N., Kerr, Y., Font, J., Martin-Neira, M., Oliva, R., Daganzo-Eusebio, E., Grant, J.P., Sabia, R., Macelloni, G., Rautiainen, K., Fauste, J., de Rosnay, P., Munoz-Sabater, J., Verhoest, N., Lievens, H., Delwart, S., Crapolicchio, R., de la Fuente, A., Kornberg, M., 2016. ESA's soil moisture and ocean salinity mission: from science to operational applications. Remote Sens. Environ. 180, 3–18.

Meesters, A.G.C.A., DeJeu, R.A.M., Owe, M., 2005. Analytical derivation of the vegetation optical depth from the microwave polarization difference index. IEEE Geosci. Remote Sens. Lett. 2 (2), 121–123.

Mo, T., Choudhury, B.J., Schmugge, T.J., Wang, J.R., Jackson, T.J., 1982. A model for microwave emission from vegetation-covered fields. J. Geophys. Res. 87 (C13), 11229–11237.

Moesinger, L., Dorigo, W., de Jeu, R., van der Schalie, R., Scanlon, T., Teubner, I., Forkel, M., 2020. The global long-term microwave vegetation optical depth climate archive (VODCA). Earth Syst. Sci. Data 12, 177–196.

Montpetit, B., Royer, A., Wigneron, J.P., Chanzy, A., Mialon, A., 2015. Evaluation of multi-frequency bare soil microwave reflectivity models. Remote Sens. Environ. 162, 186–195.

O'Neill, P.E., Chan, S., Njoku, E.G., Jackson, T., Bindlish, R., Chaubell, J., 2020. SMAP L3 Radiometer Global Daily 36 km EASE-Grid Soil Moisture, Version 7. NASA National Snow and Ice Data Center Distributed Active Archive Center, Boulder, Colorado USA. https://doi.org/10.5067/HH4SZ2PXSP6A [Data accessed on 2021.01.02].

Owe, M., de Jeu, R., Holmes, T., 2008. Multisensor historical climatology of satellite-derived global land surface moisture. J. Geophys. Res. 113, F01002.

Reichle, R., De Lannoy, G., Koster, R.D., Crow, W.T., Kimball, J.S.Q.L., 2020. SMAP L4 Global 3-hourly 9 km EASE-Grid Surface and Root Zone Soil Moisture Geophysical Data. Version 5. NASA National Snow and Ice Data Center Distributed Active Archive Center, Boulder, Colorado USA.

Saatchi, S.S., Le Vine, D.M., Lang, R.H., 1994. Microwave backscattering and emission model for grass canopies. IEEE Trans. Geosci. Remote Sens. 32 (1), 177–186.

Schwank, M., Stahli, M., Wydler, H., Leuenberger, J., Matzler, C., Fluhler, H., 2004. Microwave L-band emission of freezing soil. IEEE Trans. Geosci. Remote Sens. 42 (6), 1252–1261.

Su, Z., Wen, J., Dente, L., van der Velde, R., Wang, L., Ma, Y., Yang, K., Hu, Z., 2011. The tibetan plateau observatory of plateau scale soil moisture and soil temperature (Tibet-Obs) for quantifying uncertainties in coarse resolution satellite and model products. Hydrol. Earth Syst. Sci. 15, 2303–2316.

van der Schalie, R., de Jeu, R.A.M., Kerr, Y.H., Wigneron, J.P., Rodríguez-Fernández, N. J., Al-Yaari, A., Parinussa, R.M., Mecklenburg, S., Drusch, M., 2017. The merging of radiative transfer based surface soil moisture data from SMOS and AMSR-E. Remote Sens. Environ. 189, 180–193.

Verhoef, W., Menenti, M., Azzali, S., 1996. A colour composite of NOAA-AVHRR-NDVI based on time series analysis (1981–1992). Int. J. Remote Sens. 17, 231–235.

Vittucci, C., Ferrazzoli, P., Kerr, Y., Richaume, P., Guerriero, L., Rahmoune, R., Laurin, G. V., 2016. SMOS retrieval over forests: exploitation of optical depth and tests of soil moisture estimates. Remote Sens. Environ. 180, 115–127.

Wang, Q., van der Velde, R., Su, Z., 2018. Use of a discrete electromagnetic model for simulating aquarius L-band active/passive observations and soil moisture retrieval. Remote Sens. Environ. 205, 434–452.

Wegmüller, U., Mätzler, C., Njoku, E., 1995. Canopy opacity models, in passive microwave remote sensing of land atmosphere interactions. B. etl. Ed. Utrecht, The Netherlands: VSP, 375.

Wegmüller, U., Mätzler, C., 1999. Rough bare soil reflectivity model. IEEE Trans. Geosci. Remote Sens. 37, 1391–1395.

Wigneron, J.P., Chanzy, A., Calvet, J.C., Bruguier, N., 1995. A simple algorithm to retrieve soil moisture and vegetation biomass using passive microwave measurements over crop fields. Remote Sens. Environ. 51, 331–341.

Wigneron, J.P., Fan, L., Ciais, P., Chave, J., Brandt, M., Baccini, A., Saatchi, S., Fensholt, R., 2020. Tropical forests did not recover from the strong 2015-2016 El Nino event. Sci. Adv. 6..

Wigneron, J.P., Jackson, T.J., O'Neill, P., De Lannoy, G., de Rosnay, P., Walker, J.P., Ferrazzoli, P., Mironov, V., Bircher, S., Grant, J.P., Kurum, M., Schwank, M., Munoz-Sabater, J., Das, N., Royer, A., Al-Yaari, A., Al Bitar, A., Fernandez-Moran, R., Lawrence, H., Mialon, A., Parrens, M., Richaume, P., Delwart, S., Kerr, Y., 2017. Modelling the passive microwave signature from land surfaces: a review of recent results and application to the L-band SMOS & SMAP soil moisture retrieval algorithms. Remote Sens. Environ. 192, 238–262.

Wigneron, J.P., Kerr, Y., Waldteufel, P., Saleh, K., Escorihuela, M.J., Richaume, P., Ferrazzoli, P., de Rosnay, P., Gurney, R., Calvet, J.C., Grant, J.P., Guglielmetti, M., Hornbuckle, B., Mätzler, C., Pellarin, T., Schwank, M., 2007. L-band microwave emission of the biosphere (L-MEB) model: description and calibration against experimental data sets over crop fields. Remote Sens. Environ. 107, 639–655.

Wigneron, J.P., Laguerre, L., Kerr, Y.H., 2001. A simple parameterization of the L-MEB microwave emission model from rough agriculturral soils. IEEE Trans. Geosci. Remote Sens. 39 (8), 1697–1707.

Wigneron, J.P., Pardé, M., Waldteufel, P., Chanzy, A., Kerr, Y., Schmidl, S., Skou, N., 2004. Characterizing the dependence of vegetation model parameters on crop structure, incidence angle, and polarization at L-band. IEEE Trans. Geosci. Remote Sens. 42 (2), 416–425.

Wigneron, J.P., Li, X., Frappart, F., Fan, L., Al-Yaari, A., Lannoy, G.D., Liu, X., Wang, M., Masson, E.L., Moisy, C., 2021. SMOS-IC data record of soil moisture and L-VOD: historical development, applications and perspectives. Remote Sens. Environ. 254, 112238.

Xu, X., Dunbar, R.S., Derksen, C., Colliander, A., Kim, Y.S.K.J., 2020. SMAP L3 Radiometer Global and Northern Hemisphere Daily 36 km EASE-Grid Freeze/Thaw State. Version 3. NASA National Snow and Ice Data Center Distributed Active Archive Center, Boulder, Colorado USA.

Zhang, K., Li, X., Zheng, D., Zhang, L., Zhu, G., 2022. Estimation of global irrigation water use by the integration of multiple satellite observations. Water Resour. Res. 58 (3), e2021WR030031.

Zhang, P., Zheng, D., van der Velde, R., Wen, J., Zeng, Y., Wang, X., Wang, Z., Chen, J., Su, Z., 2021. Status of the Tibetan Plateau observatory (Tibet-Obs) and a 10-year (2009–2019) surface soil moisture dataset. Earth Syst. Sci. Data. 13, 1–28.

Zhao, T., Shi, J., Entekhabi, D., Jackson, T.J., Hu, L., Peng, Z., Yao, P., Li, S., Kang, C.S., 2021. Retrievals of soil moisture and vegetation optical depth using a multi-channel collaborative algorithm. Remote Sens. Environ. 257, 112321.

Zheng, D., van der Velde, R., Su, Z., Wang, X., Wen, J., Booij, M.J., Hoekstra, A.Y., Chen, Y., 2015. Augmentations to the Noah model physics for application to the Yellow River source area. Part I: soil water flow. J. Hydrometeorol. 16 (6), 2659–2676.

Zheng, D., van der Velde, R., Su, Z., Wen, J., Wang, X., Yang, K., 2017a. Evaluation of Noah frozen soil parameterization for application to a Tibetan meadow ecosystem. J. Hydrometeorol. 18, 1749–1763.

Zheng, D., Wang, X., van der Velde, R., Zeng, Y., Wen, J., Wang, Z., Schwank, M., Ferrazzoli, P., Su, Z., 2017b. L-band microwave emission of soil freeze–thaw process in the third pole environment. IEEE Trans. Geosci. Remote Sens. 55 (9), 5324–5338.

Zheng, D., van der Velde, R., Wen, J., Wang, X., Ferrazzoli, P., Schwank, M., Colliander, A., Bindlish, R., Su, Z., 2018a. Assessment of the SMAP soil emission

model and soil moisture retrieval algorithms for a Tibetan desert ecosystem. IEEE Trans. Geosci. Remote Sens. 56 (7), 3786–3799.

Zheng, D., Wang, X., van der Velde, R., Ferrazzoli, P., Wen, J., Wang, Z., Schwank, M., Colliander, A., Bindlish, R., Su, Z., 2018b. Impact of surface roughness, vegetation opacity and soil permittivity on L-band microwave emission and soil moisture retrieval in the third pole environment. Remote Sens. Environ. 209, 633–647.

Zheng, D., Wang, X., van der Velde, R., Schwank, M., Ferrazzoli, P., Wen, J., Wang, Z., Colliander, A., Bindlish, R., Su, Z., 2019. Assessment of soil moisture SMAP retrievals

and ELBARA-III measurements in a tibetan meadow ecosystem. IEEE Geosci. Remote Sens. Lett. 16 (9), 1407–1411.

Zheng, D., Li, X., Zhao, T., Wen, J., van der Velde, R., Schwank, M., Wang, X., Wang, Z., Su, Z., 2021a. Impact of soil permittivity and temperature profile on L-band microwave emission of frozen soil. IEEE Trans. Geosci. Remote Sens. 59, 4080–4093.

Zheng, D., Li, X., Wen, J., Hofste, J., van der Velde, R., Wang, X., Wang, Z., Bai, X., Schwank, M., Su, Z., 2021b. Active and passive microwave signatures of diurnal soil freeze-thaw transitions on the Tibetan Plateau. IEEE Trans. Geosci. Remote Sens. 60 https://doi.org/10.1109/TGRS.2021.3092411.